

Inhomogeneous superconductivity in (001), (110) and (111) KTaO_3 two-dimensional electronic gas: T_c driven from electronic confinement

Mattia Trama,^{1,2,*} Roberta Citro,^{1,2,3} and Carmine Antonio Perroni^{2,3,4,†}

¹*Physics Department “E.R. Caianiello”, Università degli Studi di Salerno, Via Giovanni Paolo II, 132, I-84084 Fisciano (Sa), Italy*

²*INFN - Sezione collegata di Salerno, Complesso Univ. Monte S. Angelo, I-80126 Napoli, Italy*

³*CNR-SPIN, I-84084 Fisciano (Salerno), Italy, c/o Università di Salerno, I-84084 Fisciano (Salerno), Italy*

⁴*Physics Department “Ettore Pancini”, Università degli Studi di Napoli Federico II, Via Cinthia, 80126-Napoli, Italy*

We investigate superconductivity in KTaO_3 (KTO)-based two-dimensional electron gases for the (001), (110), and (111) crystallographic orientations within a unified microscopic framework. Using a self-consistent tight-binding slab model, we determine the confinement potential, electronic structure, and orbital composition for each orientation, explicitly including inversion-symmetry-induced orbital Rashba couplings. Using a local spin-singlet s -wave pairing interaction, we find that the pronounced orientation dependence of the superconducting critical temperature primarily originates from differences in the spatial extent of the two-dimensional electron gas and the associated redistribution of the density of states at the Fermi level, rather than from changes in the pairing interaction. Our results provide a microscopic explanation for the experimentally observed orientation dependence of superconductivity at KTO-based interfaces.

I. INTRODUCTION

Two-dimensional electron gases (2DEGs) formed at oxide interfaces provide a fertile platform for exploring the interplay between confinement, orbital physics, spin-orbit coupling, and electronic correlations [1–10]. Among these systems, hetero-structures based on KTaO_3 (KTO) oxides have recently attracted considerable attention due to the combination of strong spin-orbit coupling inherited from the Ta $5d$ orbitals and a remarkable tunability of their electronic properties, such as superconductivity, by electrostatic gating and interface engineering [11–14].

Angle-resolved photoemission spectroscopy (ARPES) experiments have revealed that the electronic structure of KTO 2DEGs is highly sensitive to the crystallographic orientation of the interface, with distinct band dispersions and spin-orbital textures emerging for the (001), (110), and (111) directions [15]. In particular, the (111) orientation exhibits a complex multi-orbital structure associated with the trigonal symmetry of the interface, leading to unconventional spin-orbital locking and Berry curvature effects [16–22]. Even more strikingly, recent transport experiments have demonstrated the emergence of superconductivity in KTO-based interfaces, with a critical temperature that strongly depends on the crystallographic orientation [23–39]. Although superconductivity in (001)-oriented 2DEGs emerges only within a limited range of experimental conditions (see Refs. [27, 28]), the magnitude of T_c and its dependence on carrier density display substantial quantitative differences between the (110) and (111) interfaces. Understanding the microscopic origin of this anisotropy remains an open theoretical challenge. In particular, it remains unclear whether the hierarchy of T_c reported in Refs. [23–25] requires

orientation-dependent pairing interactions or can instead be explained purely in terms of geometric confinement and multi-orbital electronic structure [32].

From a theoretical perspective, the electronic properties of oxide 2DEGs are governed by a delicate balance between quantum confinement, orbital-dependent hoppings, and electrostatic screening. Previous studies have shown that the confinement potential at KTO interfaces is highly non-trivial and strongly affected by the dielectric response of the host material [18, 19]. As a result, different crystallographic orientations can host qualitatively different layer-resolved charge distributions and orbital occupancies, even at comparable total carrier densities.

In this work, we investigate superconductivity in KTO-based 2DEGs for the (001), (110), and (111) crystallographic orientations within a unified microscopic framework. Starting from a self-consistent tight-binding description of the electronic structure in slab geometry, we determine the confinement potential and the resulting band structure for each orientation, explicitly accounting for orbital Rashba couplings induced by inversion symmetry breaking [20, 40]. We then introduce a local spin-singlet s -wave pairing interaction and analyze inhomogeneous superconductivity at the mean-field level, keeping the same microscopic interaction strength for all geometries, in order to study the effect of the different orientations.

The approach used in the paper allows to disentangle the role of confinement, orbital composition, and density of states in shaping the superconducting instability across different orientations. Our results show that the orientation dependence of superconductivity primarily originates from differences in the spatial extension of the 2DEG and the associated redistribution of the low-energy density of states, rather than from changes in the pairing interaction itself. These findings provide a coherent theoretical interpretation of the experimentally

* mtrama@unisa.it

† carmine.perroni@unina.it

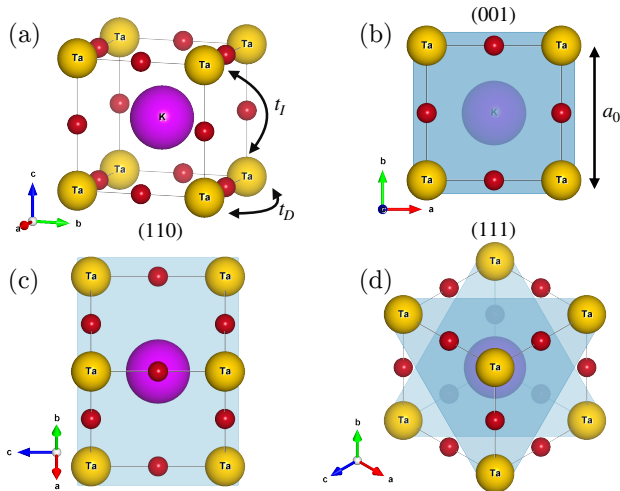


Figure 1. (a) Cubic structure of KTO; t_D and t_I denote the tight-binding hopping amplitudes. (b–d) Top view of crystalline KTO along the (001) (b), (110) (c), and (111) (d) directions. The cubic lattice constant is $a_0 = 3.988 \text{ \AA}$.

observed anisotropy of superconductivity in KTO interfaces and highlight the crucial role of orbital physics in oxide-based superconductors.

The paper is organized as follows. In Sec. II, we discuss the electrostatic potential and the electronic band structure for different crystallographic directions, in Sec. III we focus on the superconducting instability evaluating the related critical temperature, and in Sec. IV there are conclusions and a final discussion. Five Appendices close the paper: Appendix A details the orbital Rashba terms for different crystallographic, Appendix B the dielectric function orientations, Appendix C the bulk limit, Appendix D the approach to inhomogeneous superconductivity, and Appendix E additional details on the role of spatial extension of the superconducting order parameter.

II. ELECTROSTATIC POTENTIAL AND ELECTRONIC BAND STRUCTURE

To investigate the role of different crystallographic orientations, in this section, we consider a model in which all microscopic parameters are kept fixed as much as possible. In this way, the results are not biased by orientation-dependent details of the 2DEG formation.

We start from an ideal cubic system so that the orientation mainly affects (i) the projection of the bulk dispersion onto the surface Brillouin zone (BZ), and (ii) the symmetry of the low-energy distortions. Fig. 1 illustrates the cubic structure of KTO and its atomic arrangement viewed along the (001), (110), and (111) crystallographic directions. The different projections highlight how the same cubic lattice generates distinct in-plane geometries and symmetries at the interface. In particular, while the (001) surface preserves a square

symmetry, the (110) and (111) orientations lead to different symmetries and modified orbital overlap patterns. These geometric differences play a crucial role in shaping the electronic confinement, orbital composition, and ultimately the superconducting properties discussed in the following section.

We describe the bulk electronic structure within a tight-binding model [21].

We label the t_{2g} orbitals by $\alpha \in \{1, 2, 3\} = \{x, y, z\}$, corresponding to (d_{yz}, d_{zx}, d_{xy}) .

The bulk Hamiltonian reads

$$H_{\text{TB}}^{\text{Bulk}} = \sum_{\mathbf{K}} \sum_{\alpha \sigma} \left[-t_D \sum_{\beta} (1 - \delta_{\alpha\beta}) \cos(K_{\beta}) - t_I \cos(K_{\alpha}) \right] c_{\mathbf{K}\alpha\sigma}^{\dagger} c_{\mathbf{K}\alpha\sigma}. \quad (1)$$

where t_D and t_I denote the nearest-neighbor (NN) and next-to-nearest-neighbor (NNN) hopping amplitudes, respectively. The operator $c_{\mathbf{K}\alpha\sigma}$ annihilates an electron with crystal momentum \mathbf{K} , orbital α , and spin σ . The momentum \mathbf{K} is expressed in Cartesian coordinates, with components K_{α} measured in units of $1/a_0$, where $a_0 = 3.988 \text{ \AA}$ is the cubic lattice constant of KTO. For each crystallographic direction, we rotate the coordinate system and discretize the Hamiltonian along the direction transverse to the interface [21], according to the structures shown in Fig. 1. Fixed the plane, for which translational invariance is preserved, we denote by $\mathbf{k} = (k_x, k_y)$ its quasi-momentum (in units of the inverse of in-plane lattice constants) and by z the corresponding transverse direction. We include the atomic spin-orbit coupling H_{SOC} in the form

$$H_{\text{SOC}} = \frac{\lambda}{2} \sum_{\mathbf{k}} \sum_{z \alpha \beta \gamma \sigma \sigma'} i \varepsilon_{\alpha\beta\gamma} c_{\mathbf{k}z\alpha\sigma}^{\dagger} \sigma_{\sigma\sigma'}^{\gamma} c_{\mathbf{k}z\beta\sigma'}, \quad (2)$$

where $\lambda \approx 0.27 \text{ eV}$ [18].

For each slab orientation, we also consider a $\mathbf{k} = 0$ perturbation H_{dist} describing crystal-field distortions:

$$H_{\text{dist}}^{(001)/(110)} = \frac{\delta}{2} \sum_{\mathbf{k}} \sum_{z \sigma} c_{\mathbf{k}z3\sigma}^{\dagger} c_{\mathbf{k}z3\sigma}, \quad (3)$$

$$H_{\text{dist}}^{(111)} = \frac{\delta}{2} \sum_{\mathbf{k}} \sum_{z \alpha \neq \beta \sigma} c_{\mathbf{k}z\alpha\sigma}^{\dagger} c_{\mathbf{k}z\beta\sigma}, \quad (4)$$

corresponding to tetragonal and trigonal crystal fields, respectively. We set $\delta = -10 \text{ meV}$, a typical magnitude for such distortions [22]. For the (001) and (110) orientations this distortion is typically negligible, since the d_{xy} orbital is already split from d_{yz} and d_{zx} . In contrast, for the (111) orientation the trigonal field lifts the orbital degeneracy, leading to qualitative changes in the low-filling band structure.

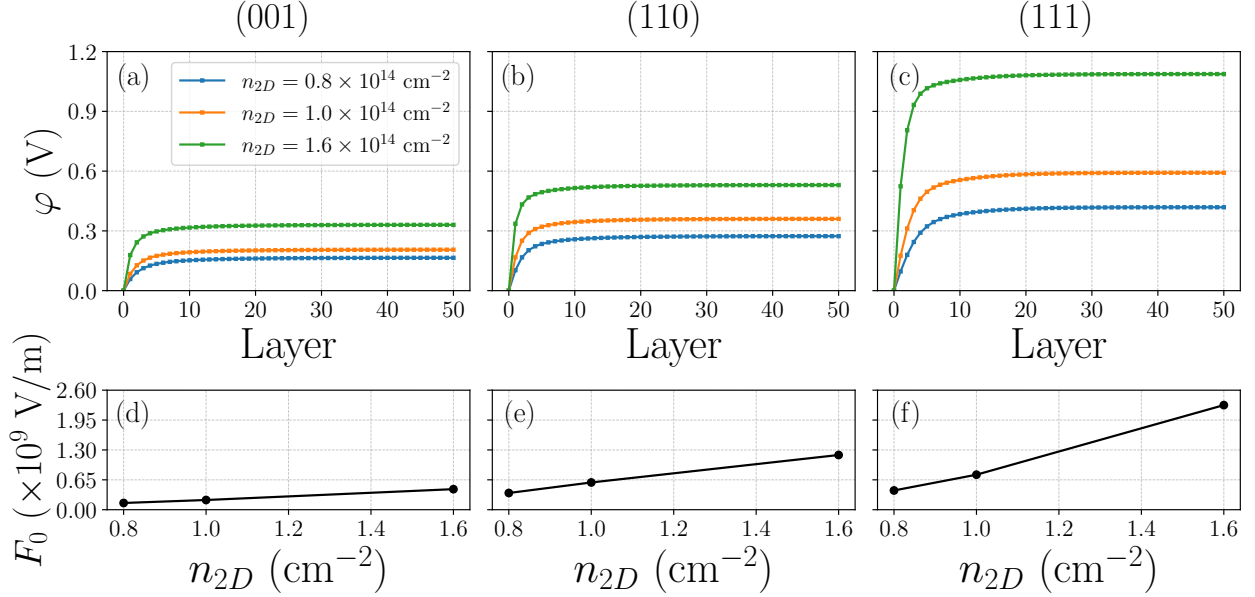


Figure 2. (a-c) Potential barrier φ as a function of the layer position using different benchmark values of the positive charge density n_{2D} for the (001) (a), (110) (b) and (111) (c) directions. (d-f) Interfacial electric field F_0 as a function of n_{2D} for (001) (d), (110) (e) and (111) (f) directions.

Finally, we introduce a z -dependent electrostatic potential describing confinement at the interface

$$H_\varphi = \sum_{\mathbf{k}} \sum_{z \alpha \sigma} \varphi(z) c_{\mathbf{k}z\alpha\sigma}^\dagger c_{\mathbf{k}z\alpha\sigma}, \quad (5)$$

where $\varphi(z)$ is determined self-consistently. The term in Eq. (5) breaks inversion symmetry, leading to the emergence of the orbital Rashba effect [18–20]. Its amplitude is proportional to the electric field at each layer and couples different layers. In Appendix A we describe both NN and NNN Rashba hoppings arising along all three crystallographic directions. Unlike simplified monolayer or four-band models commonly used for (001) and (111) interfaces, we include all couplings up to NNN.

In order to ensure a consistent comparison among interfaces, we adopt a common set of benchmark parameters. We fix the hopping amplitudes t_D and t_I of Eq. (1) using the (111) slab as a reference. From ARPES data [15] combined with an effective electrostatic potential model [18], we extract $t_D = 0.39$ eV and $t_I = 0.015$ eV. The self-consistent electric potential is obtained through the iterative scheme described in Ref. [21]. The procedure couples the electronic density n_z , computed from the squared modulus of the layer-resolved wave functions after diagonalization to the discrete Maxwell equations along the finite direction:

$$\begin{cases} \varphi(z) = -a' \sum_{l=1}^z F_l, \\ \varepsilon_0 \varepsilon(F_z) F_z = D_z, \\ D_z = |e|(n_{2D} - \sum_{l=1}^z n_l), \end{cases} \quad (6)$$

where a' is the interlayer spacing along the z direction and n_{2D} the positive interface charge density, treated as a free parameter and screened by the electronic charge in the slab. To close the problem, we specify the dielectric function $\varepsilon(F_z)$ governing screening along the slab, where F_z is the electric field at the z -th layer. The fitting procedure is detailed in Appendix B. We adopt the best-fit expression capturing the low-temperature ferroelectric behavior [33, 41],

$$\varepsilon(F) = 1 + \frac{\chi_0}{\left(1 + \frac{F^2}{F_c^2}\right)^{1/3}}, \quad (7)$$

with $\chi_0 = 3600$ and $F_c = 443.7$ kV/m.

Having defined the model, we now describe the equilibrium 2DEG emerging from the substrate. This requires reaching the bulk limit, namely $F_{N_L} = 0$, where N_L denotes the number of layers in the slab, for any $N_L > N_{\text{crit}}$. In Appendix C we analyze this convergence and find $N_{\text{crit}} \approx 41$ for the largest value of n_{2D} considered. To ensure full convergence, we set $N_L = 51$ in all calculations.

Here we discuss, for the three different crystallographic directions, the electrostatic potential and the resulting band structure. In Fig. 2 we show, for the three different orientations, the evolution of the electrostatic potential (upper panels) and the electric field (lower panels) with varying the distance from the interface, for several benchmark values of the positive density n_{2D} . We observe that the electric field increases by moving from the (001) to the (110), finally to the (111) interface, up to a factor of four for the largest values of particle density n_{2D} of the positive charge at the interface.

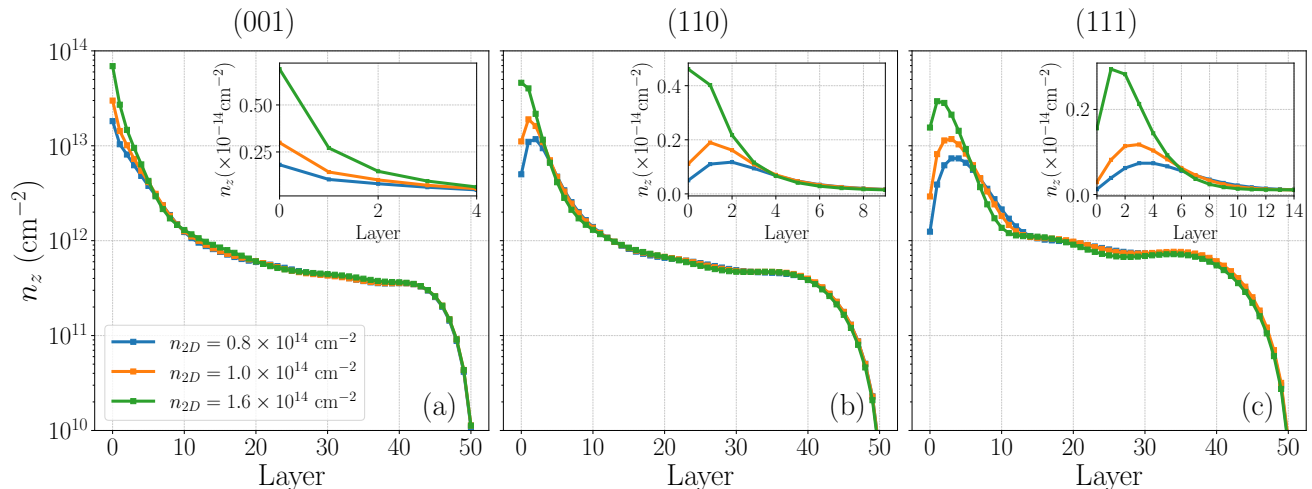


Figure 3. Electron 2D density n_z for different benchmark values of n_{2D} at the (001) (a), (110) (b) and (111) (c) interfaces. The insets show the details close to the interfaces.

We find that the steepest electrostatic barrier forms along the (111) direction, despite the corresponding 2DEG being less spatially confined. This nontrivial behavior originates from the predominance of out-of-plane hopping processes in the (111) orientation, in contrast to the (001) and (110) cases, where stronger in-plane dispersion naturally favors localization near the interface. The competition between electronic screening and anisotropic dispersion results in a stronger electric field at the (111) interface.

On the other hand, as one can observe in Fig. 3, the electronic density as function of the layer position shows that 2DEG confinement is stronger in the (001) interface, which is characterized by the more in-plane electronic dispersion. Roughly, one can say that the number of layers for which the 2DEG is confined is $\Delta N_{001} = 2$ for the (001) interface, $\Delta N_{110} = 5$ for the (110) interface, and $\Delta N_{111} = 10$ for the (111) interface. In particular, for the lowest considered densities of the (110) and for all the considered densities of the (111) interface, the localization occurs mostly shifted from the very first layer, having a peak for $N_l \neq 0$. We also notice that the electronic density of the 2DEG does not correspond to the total positive density n_{2D} . Indeed, if for the (111) interface we need to include $n_{2D} = 1.6 \times 10^{14} \text{ cm}^{-2}$ to make the 2DEG density of the order of $1.0 \times 10^{14} \text{ cm}^{-2}$, for the (001) interfaces, this value is mostly saturated in the 2DEG itself. However, this is in contrast with the experimental observation of 2DEG with less electronic density for the (001) and (110) interfaces [23]. This means that we might compare the three different interfaces by choosing different positive densities n_{2D} . Fig. 4 displays the electronic band structure of the KTO-based slab for the three crystallographic orientations and for different values of the positive interface density n_{2D} . Energies are measured relative to the self-consistent chemical potential determined from the electrostatic

screening procedure, such that $E = 0$ corresponds to the Fermi level at each n_{2D} . The projection of the bulk t_{2g} manifold onto the corresponding surface Brillouin zones produces markedly different dispersions depending on the interface orientation. For the (001) configuration, the bands exhibit a relatively stronger in-plane dispersion and a more clearly resolved confinement-induced subband structure. In contrast, the (110) and, even more prominently, the (111) orientations display a richer multi-orbital structure with enhanced band mixing and reduced effective confinement effects. Notably, even in the most localized (001) case, the chemical potential intersects bands belonging to the bulk continuum.

Fig. 5 shows the local layer-resolved density of states (LDOS) evaluated at the self-consistent chemical potential for different values of the positive interface density n_{2D} and for the three crystallographic orientations. The LDOS is computed as

$$\text{LDOS}(z) = \sum_n \int \frac{d^2\mathbf{k}}{4\pi^2} \delta(E_{n\mathbf{k}}) |c_{\mathbf{k}z\alpha\sigma}|^2, \quad (8)$$

where $E_{n\mathbf{k}}$ denotes the n -th band energy measured relative to the self-consistent chemical potential. In practice, the Dirac delta function is approximated by a Lorentzian broadening, $\pi\delta(x) \approx \tau/(x^2 + \tau^2)$, with $\tau = 10^{-3} \text{ eV}$. The spatial distribution of the low-energy spectral weight reflects the different confinement regimes already observed in the charge-density profiles. For the (001) orientation, the density of states is strongly localized within the first few layers, consistent with the short spatial extension of the 2DEG. In contrast, the (110) configuration exhibits a broader distribution extending over several layers, while the (111) orientation displays the most spatially extended profile, with substantial spectral weight distributed deeper into the slab.

The distinct band topologies and Fermi surface structures emerging in the three geometries directly influence

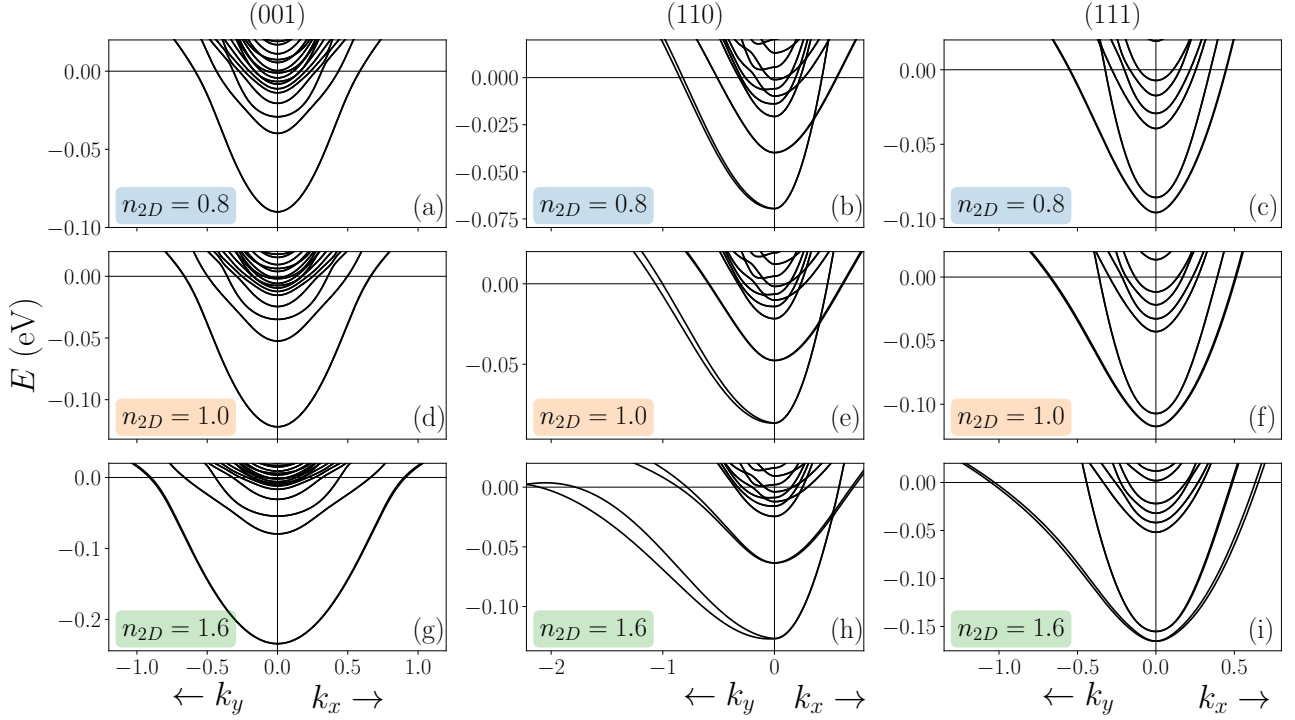


Figure 4. Band structure of the KTO-based heterostructure along the (a,d,g) (001), (b,e,h) (110), and (c,f,i) (111) directions for positive charge densities (a–c) $n_{2D} = 0.8 \times 10^{14}, \text{cm}^{-2}$, (d–f) $n_{2D} = 1.0 \times 10^{14}, \text{cm}^{-2}$, and (g–i) $n_{2D} = 1.6 \times 10^{14}, \text{cm}^{-2}$. The quasi-momentum k_i is expressed in units of the corresponding in-plane lattice constant. The energy zero ($E = 0$) is set to the self-consistent Fermi level obtained from the electrostatic screening simulations at each n_{2D} .

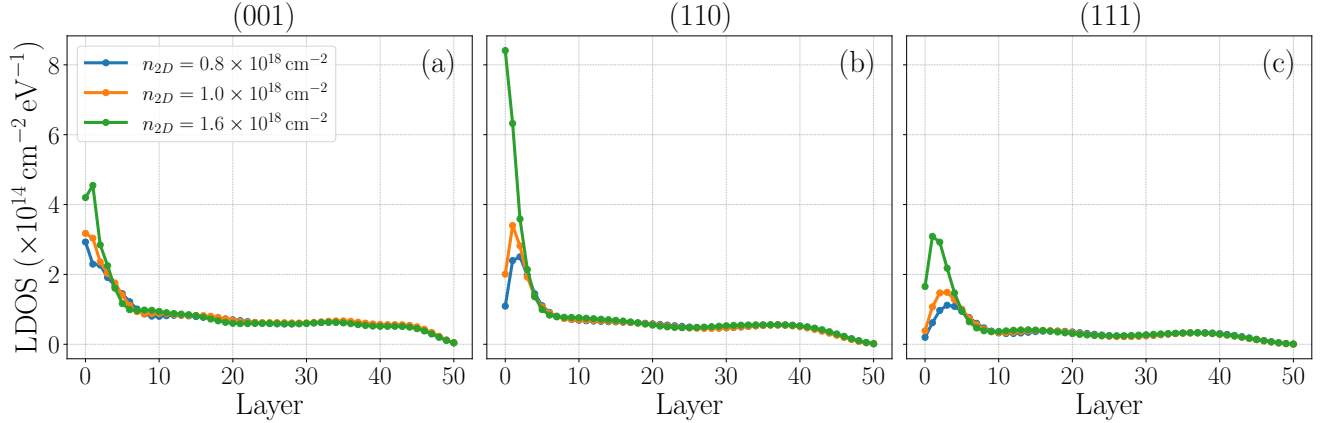


Figure 5. (a–c) Local layered-resolved density of states at the self-consistent value of the chemical potential for (001) (a), (110) (b) and (111) (c) directions.

the density of states at the Fermi level and its spatial distribution across the slab. As discussed in the following section, these orientation-dependent electronic features play a central role in establishing the hierarchy of superconducting critical temperatures among the (001), (110), and (111) interfaces. Indeed, the broader spatial distribution characterizing the (111) interface enhances the weighted density of states entering the instability condition, thereby favoring a higher critical temperature compared to the (001) and (110) cases.

III. SUPERCONDUCTING INSTABILITY AND CRITICAL TEMPERATURE

In this section we investigate the emergence of the superconducting instability in the three orientations: (001), (110) and (111).

Starting from a bulk three-dimensional description of a local attractive four-fermion Hamiltonian, inhomogeneous superconductivity is described within a mean-field approximation as

$$H_S = -U \sum_{\mathbf{k} \in \frac{1}{2}\text{BZ}} \sum_{z \alpha} \left(\Delta_z c_{\mathbf{k}z\alpha\uparrow}^\dagger c_{-\mathbf{k}z\alpha\downarrow}^\dagger + \text{h.c.} \right) + \mathcal{A} \sum_z U \Delta_z^2, \quad (9)$$

where $\Delta_z = \langle c_{iz\alpha\uparrow} c_{iz\alpha\downarrow} \rangle$. Here i denotes the in-plane real-space coordinate, \mathbf{k} the in-plane quasi-momentum, z the coordinate perpendicular to the interface, α the orbital index, and σ the spin. The parameter U represents the effective pairing interaction strength, encoding the microscopic origin of superconductivity, and it is taken to be the same for all slab configurations. Finally, \mathcal{A} accounts for the different in-plane unit-cell areas associated with the various interface orientations. This factor ensures that the superconducting instability is compared across different geometries under equivalent conditions, i.e. with U expressed in the same units for all three configurations. In Appendix D, we report details of the inhomogeneous mean-field approach.

In the following, we consider two opposite pairing regimes, which should be regarded as lower and upper bounds for the predicted T_c within this singlet s -wave model. In the first case, the energy U is taken to be nonzero only within an energy shell of width $\hbar\omega_i$ around the Fermi level, where ω_i is a characteristic frequency scale typical of phonon-mediated superconductivity (e.g., the Debye frequency or frequency of soft modes [23, 42]). In the second case, U is assumed to be constant over the entire energy range, corresponding to an instantaneous (non-retarded) pairing mechanism. Even in the latter case, the contribution of electrons forming Cooper pairs decreases logarithmically away from the Fermi level, ensuring that states close to E_F still dominate the superconducting instability. In the following, we refer to these two models as the *phonon-mediated* and the *instantaneous* pairing mechanisms, respectively.

In Eq.(9), the order parameter Δ_z is explicitly allowed to depend on the transverse coordinate z , while being assumed homogeneous in-plane and independent of the orbital index. This choice reflects the presence of the confining potential, which breaks translational invariance along z and induces a spatial dependence of the superconducting order parameter. We adopt a variational approach introducing an ansatz for the order parameter of the form

$$\Delta_z = \Delta e^{-z/z_0}, \quad (10)$$

where Δ and z_0 are the two variational parameters describing the amplitude and the spatial penetration depth of the superconducting pairs across the bulk, respectively. This choice ensures the recovery of the standard homogeneous Bardeen-Cooper-Schrieffer (BCS) order parameter in the limit $z_0 \gg N_L$. We notice that the exponential ansatz provides the minimal smooth profile compatible with broken translational symmetry along the confinement direction, while avoiding over-parametrization. We have verified that alternative smooth profiles lead to qualitatively identical results for the critical temperatures.

In order to determine the self-consistent values of the variational parameters, we minimize the variation of the free-energy functional $F = F_S - F_N$ of the free energies in the superconducting and the normal state, which can be written as

$$F = 3U \sum_{z=0}^{N_L-1} \Delta^2 e^{-2z/z_0} - \frac{\mathcal{P}}{\beta} \sum_n \int d^2\mathbf{k} [\log(2 + 2 \cosh(\beta\lambda_{n\mathbf{k}})) - \log(2 + 2 \cosh(\beta E_{n\mathbf{k}}))], \quad (11)$$

where $\beta = 1/k_B T$, the factor 3 explicitly accounts for the three orbital degrees of freedom, \mathcal{P} is a geometry-dependent constant (see Appendix D for details), and n runs over the normal-state electronic bands. The Bogoliubov-de Gennes (BdG) eigenvalues are given by

$$\lambda_{n\mathbf{k}} = \sqrt{E_{n\mathbf{k}}^2 - U^2 \Delta^2 f_{\mathbf{k}}^2(z_0)}, \quad (12)$$

where

$$f_{\mathbf{k}}(z_0) = \sum_{z \alpha \sigma} |c_{\mathbf{k}z\alpha\sigma}|^2 e^{-z/z_0}, \quad (13)$$

is a form factor that weights the projection of the normal-state eigenvectors across the slab. It follows from expressing Hamiltonian (9) in the eigenbasis of the normal-state Hamiltonian and reflects the chosen variational ansatz (see Ref. [43] for details).

At this stage, the value of U has not been fixed. Since we are interested in the superconducting instability, we instead determine the value of U required to produce a given critical temperature. In the limit $\Delta \rightarrow 0$, Eq. (11) simplifies to

$$F = G^2 \left(\frac{\Xi(z_0)}{U} - \Gamma(z_0) \right), \quad (14)$$

where $G = U\Delta$ is the superconducting gap opened at the first layer of the interface, and

$$\Xi(z_0) = 3 \frac{1 - e^{-2N_L/z_0}}{1 - e^{-2/z_0}}, \quad (15)$$

$$\Gamma(z_0) = \frac{\mathcal{P}}{2} \sum_n \int d^2\mathbf{k} \tanh\left(\frac{\beta E_{n\mathbf{k}}}{2}\right) \frac{f_{\mathbf{k}}^2(z_0)}{E_{n\mathbf{k}}}. \quad (16)$$

Here we have explicitly performed the summation over z in Eq. (15).

Starting from Eq. (14), the critical temperature T_c can be obtained for the two pairing scenarios. Close to T_c , the relevant conditions are

$$\frac{\partial^2 F}{\partial G^2} = 0, \quad \frac{\partial F}{\partial z_0} = 0,$$

which ensure the onset of the instability and the minimization of the free energy with respect to z_0 .

A. Phonon-mediated pairing mechanism

In the case of a phonon-mediated pairing mechanism, only states within a narrow energy shell of width ω_i around the Fermi level contribute to superconductivity. Within this approximation, Eq. (16) can be written as

$$\Gamma(z_0) \approx \frac{\mathcal{P}}{2} \rho(z_0) \int_{-\omega_i}^{\omega_i} \frac{dE}{E} \tanh\left(\frac{\beta E}{2}\right), \quad (17)$$

where

$$\rho(z_0) = \sum_n \int d^2\mathbf{k} \delta(E_{n\mathbf{k}}) f_{\mathbf{k}}^2(z_0) \quad (18)$$

is the density of states at the Fermi level weighted by the factor $f_{\mathbf{k}}(z_0)$. This corresponds to a generalization of the standard BCS assumption that the density of states varies slowly within the relevant energy window, extended here to the inhomogeneous case. Under this assumption, the integral in Eq. (17) can be evaluated analytically, yielding

$$\Gamma(z_0) = \frac{\mathcal{P}}{2} \rho(z_0) \Phi\left(\frac{\beta\omega_i}{2}\right), \quad (19)$$

where $\Phi(x) \approx 2 \log(2.27x)$.

The condition $T = T_c$ reads

$$U = \frac{2}{\mathcal{P}\Phi(\beta\omega_i/2)} \min_{z_0} \left(\frac{\Xi(z_0)}{\rho(z_0)} \right), \quad (20)$$

or, equivalently,

$$\begin{cases} k_B T_c = 1.13 \omega_i \exp\left(-\frac{\tilde{U}}{2U}\right), \\ \tilde{U} = \frac{2}{\mathcal{P}} \min_{z_0} \left(\frac{\Xi(z_0)}{\rho(z_0)} \right). \end{cases} \quad (21)$$

This expression allows us to determine T_c for the different interface orientations by varying U while keeping the characteristic phonon frequency fixed. In this way, differences in T_c arise purely from electronic properties. Within this framework, the resulting critical temperatures should therefore be regarded as a lower bound for phonon-mediated superconductivity. We use $\hbar\omega_i = 10$ meV as a representative phonon energy scale. In principle, however, the characteristic frequency ω_i may also depend on the interface orientation [23, 24].

The predicted critical temperature as a function of the interaction strength U is shown in Fig. 6 for representative values of the positive interface charge density n_{2D} and for all three orientations. The corresponding self-consistent values of the penetration length z_0 are indicated at the end of each curve.

At fixed electronic density, a clear hierarchy emerges among the three orientations: the (111) interface exhibits the highest T_c and the largest penetration length, while the (001) orientation shows the lowest critical temperature, namely

$$T_c^{(001)} < T_c^{(110)} < T_c^{(111)}.$$

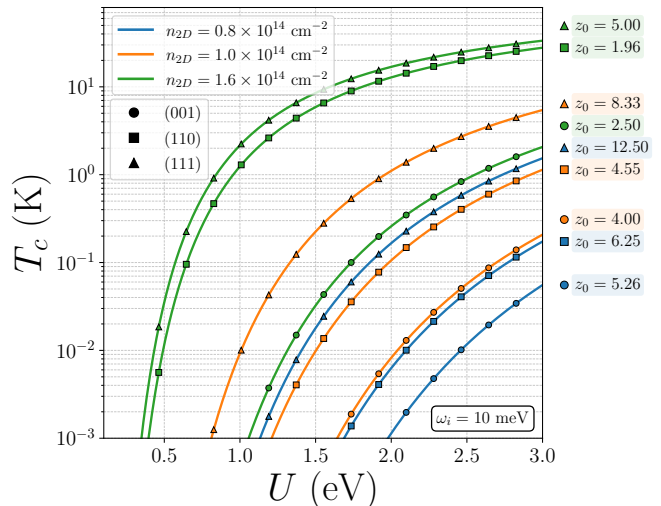


Figure 6. Critical temperature T_c as a function of the interaction strength U for the (001) (circles), (110) (squares), and (111) (triangles) crystallographic orientations, at representative values of the positive interface charge density n_{2D} . The corresponding self-consistent penetration length z_0 is indicated at the end of each curve. We use $\hbar\omega_i = 10$ meV as a representative phonon energy scale.

Moreover, at fixed density, there exists a range of interaction strengths for which $T_c^{(111)} \approx 1$ K, $T_c^{(110)} \approx 0.1$ K, while the (001) interface does not display a superconducting instability within accessible temperatures, consistent with experimental data in Refs. [23, 24].

If one also considers that the carrier density may differ among the various orientations — with the (111) interface typically hosting the largest two-dimensional electron density — the relevant range of U leading to observable superconductivity can be further enlarged.

Finally, increasing the electronic density, and therefore the electrostatic confinement potential, leads to a reduction of the optimal penetration length z_0 , in direct analogy with the shrinking spatial extension of the 2DEG in the normal state.

For completeness, we note that if the order parameter were artificially constrained to be homogeneous across the slab (i.e., $z_0 \rightarrow \infty$), a different behavior of T_c would emerge, highlighting the necessity of properly accounting for the spatial profile of the order parameter (see Appendix E for details). This behavior is driven by the corresponding differences in the density of states at the Fermi level (see Fig. 4).

B. Instantaneous pairing mechanism

We now consider an alternative pairing scenario in which U is assumed to be constant over the entire energy range, corresponding to an instantaneous (non-retarded) interaction without an energy cut-off. Within the present framework, this case provides an upper bound for the

superconducting instability, as the full electronic bandwidth contributes to pairing. The resulting T_c therefore reflects purely electronic properties of the system. This scenario is particularly relevant when the chemical potential approaches regions of strong band reconstruction or band folding. As shown in Fig. 4(g), states near the Brillouin zone boundary may become involved, making the assumption of a sharp frequency cut-off less robust.

In this case, the density of states cannot be separated from the energy integration as in the phonon-mediated scenario. However, Eq. (14) still allows for a semi-analytical minimization procedure. The condition for a minimum with respect to z_0 reads

$$\frac{\Xi'(z_0)}{U} - \Gamma'(z_0) = 0, \quad (22)$$

where the prime denotes differentiation with respect to z_0 .

Combining Eq. (22) with the instability condition $\partial^2 F / \partial G^2 = 0$, we obtain the coupled equations determining U and z_0 at $T = T_c$:

$$\begin{cases} \partial_{z_0} \log \left(\frac{\Xi}{\Gamma} \right) = 0, \\ U = \frac{\Xi}{\Gamma}. \end{cases} \quad (23)$$

In Fig. 7 we show the resulting critical temperature T_c as a function of the interaction strength U within this cutoff-free pairing model. Even in this case, allowing the order parameter to penetrate inhomogeneously into the slab reproduces the hierarchy found in the phonon-mediated scenario: at fixed density, the (111) orientation exhibits the most favorable superconducting instability and the highest T_c .

In contrast to the phonon-mediated case, the dependence of T_c on U is not purely exponential at small interaction strengths. In particular, the (001) interface displays a threshold-like behavior, which disfavors the onset of superconductivity. For sufficiently large U , however, the curves recover an exponential dependence, consistent with the asymptotic behavior obtained using the phonon-mediated pairing and discussed in the Appendix E. The amplitudes, on the other hand, differ among the three orientations, as they are determined solely by the normal-state electronic structure.

We also observe that there exists a range of interaction strengths yielding critical temperatures of the correct experimental order of magnitude for all three orientations. In Fig. 7(a), the shaded region highlights this interval at fixed density. In panel (b), the experimentally observed hierarchy is recovered only when different carrier densities are considered for the three interfaces.

For completeness, Appendix E reports the self-consistent values of z_0 . In contrast to the phonon-mediated case, z_0 now depends explicitly on U (and therefore on T_c). Moreover, there is no longer a direct correspondence between z_0 and the spatial extension of the 2DEG in the normal state, since electronic states far

from the Fermi surface — including bulk-like states — contribute nontrivially to the superconducting instability.

IV. CONCLUSIONS AND DISCUSSION

In this work we have systematically investigated the superconducting instability arising from the electronic properties of the 2DEG at (001), (110), and (111) KTaO_3 -based interfaces. To isolate the role of crystallographic orientation, we have employed a tight-binding model with identical bulk hopping amplitudes for all three geometries. The self-consistent confining potential has been computed for a large number of layers, using the same dielectric function fitted to experimental ARPES data and considering representative values of the positive interface density n_{2D} .

In the normal state, the (111) orientation exhibits the steepest electrostatic barrier, even though its 2DEG is less spatially confined. This unusual behavior arises from dominant out-of-plane hopping, unlike the (001) and (110) orientations where stronger in-plane dispersion promotes interface localization. The interplay between electronic screening and anisotropic dispersion ultimately produces a stronger electric field at the (111) interface.

We have studied the onset of superconductivity using an inhomogeneous mean-field singlet s -wave pairing interaction. Allowing the superconducting order parameter to vary across the slab, we reproduce the experimentally observed hierarchy of critical temperatures, with the (111) orientation consistently displaying the highest T_c . This hierarchy is robust across two limiting pairing scenarios: a phonon-mediated (retarded) mechanism and a local instantaneous (non-retarded) interaction, which have provided lower and upper bounds for the superconducting instability within our model. In particular, in the retarded case the results do not depend sensitively on the choice of cut-off frequency, further supporting the geometric origin of the predicted hierarchy. Importantly, this behavior of critical temperatures does not simply follow the magnitude of the interfacial electric field, but rather the spatial redistribution of low-energy spectral weight across the slab. This highlights the central role of geometric confinement and multiorbital band structure in determining superconducting instabilities in oxide-based 2DEGs.

Both the normal-state analysis and the superconducting treatment have allowed us to isolate the effects arising purely from geometric constraints and electronic structure, without introducing orientation-dependent microscopic parameters. In realistic systems, however, additional effects may further enhance the differences among orientations. For example, different surface orientations may involve distinct impurity concentrations or low-temperature lattice distortions, effectively modifying the material parameters [23, 24]. These include possible variations in effective hopping amplitudes, dielectric response, and phonon spectra, as well as different car-

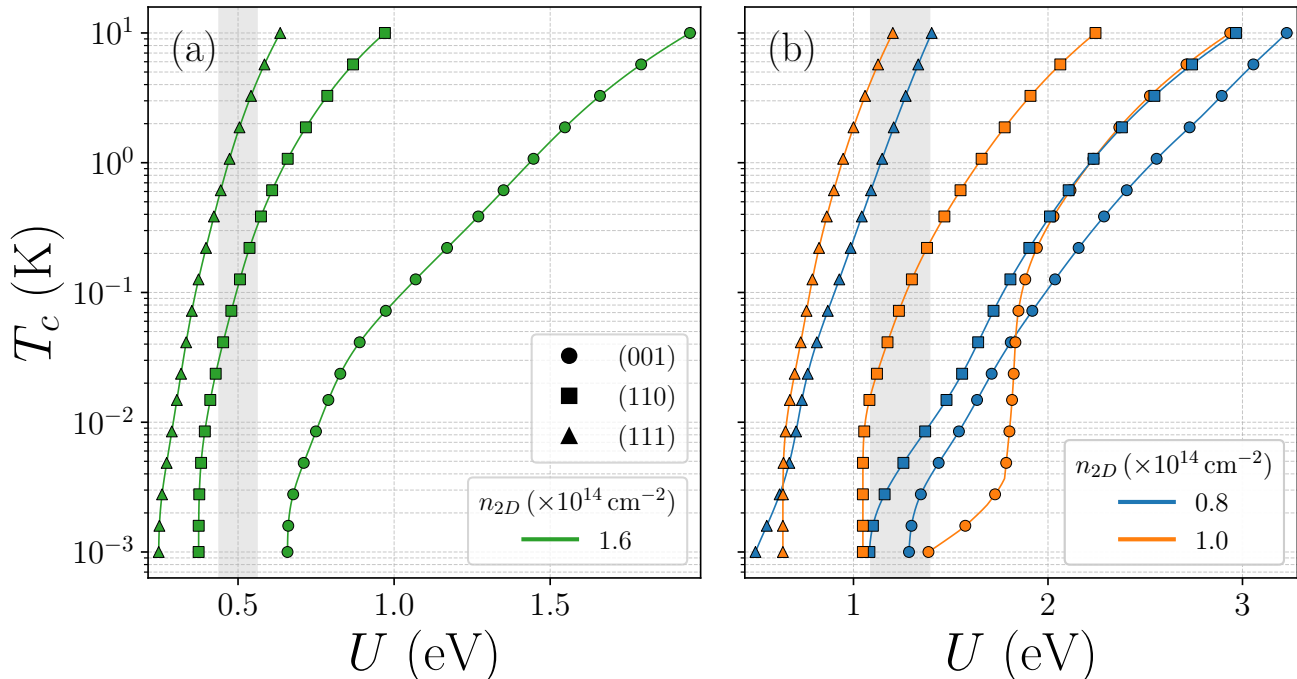


Figure 7. (a) Critical temperature T_c as a function of the interaction strength U for $n_{2D} = 1.6 \times 10^{14} \text{ cm}^{-2}$. (b) Same quantity for $n_{2D} = 0.8 \times 10^{14} \text{ cm}^{-2}$ (blue) and $n_{2D} = 1.0 \times 10^{14} \text{ cm}^{-2}$ (orange). Different markers denote different crystallographic orientations: circles (001), squares (110), and triangles (111). The gray area highlights the region of U which are able to reproduce the experimental order of magnitude of T_c .

rier densities - with the (111) interface typically hosting the largest 2DEG density - all of which could affect the hierarchy in T_c predicted here.

Finally, our analysis has been restricted to singlet s -wave pairing. Although alternative pairing symmetries have been proposed for KTO-based systems [13, 36, 39], s -wave pairing is expected to remain the most robust channel in the experimentally relevant dirty regime, where higher-angular-momentum components are typically suppressed. More generally, the present framework is not tied to a specific symmetry of the order parameter. Its central ingredients—namely the multi-orbital electronic structure and the finite dispersion along the z direction—govern the spatial extension of the 2DEG at the interface. These elements directly enter the determination of the superconducting instability, since they control both the spatial distribution of the condensate and the structure of the pairing kernel.

The formalism can be straightforwardly generalized to other pairing symmetries [44], allowing one to investigate how the symmetry of the order parameter modifies its spatial profile and the resulting instability, both in the static and in the dynamic regime [45, 46]. In this perspective, the 2DEG confinement naturally enters the determination of the superconducting properties of the system, independently of the specific symmetry of the pairing channel, as it controls the spatial structure of the electronic states participating in the pairing.

ACKNOWLEDGMENT

M.T. and R.C. acknowledge Nicolas Bergeal, Hugo Witt, Andrea Caviglia, Ulderico Filippozzi, Arun Kumar Jaiswal, Francesco Romeo, Claudio Guarcello, Alfonso Maiellaro and Roberto Capecelatro for fruitful discussions. The authors acknowledge funding from IQARO (Spinorbitronic Quantum Bits in Reconfigurable 2DOxides) project of the European Union’s Horizon Europe research and innovation programme under grant agreement n. 101115190. C.A.P. acknowledges funding from the PRIN 2022 PNRR project P2022SB73K “Superconductivity in KTaO3 Oxide-2DEG NAnodevices for Topological quantum Applications” (SONATA) financed by the European Union - Next Generation EU. R.C. acknowledges support from the PNRR MUR Project No. PE0000023-NQSTI (TOPQIN and SPUNTO) and from the project INNOVATOR (National centre HPC, big data and quantum computing). M.T. acknowledges PNRR MUR Project No. PE0000023-NQSTI (SOC-OX CUP E63C22002180006).

Appendix A: Orbital Rashba terms for different orientations

In this Appendix we derive the matrices describing the orbital Rashba coupling arising from inversion-symmetry breaking along the (001), (110), and (111) crystallo-

graphic directions.

In simplified 2D treatments, the orbital Rashba term is often written, for the (001) interface, in the form

$$h^{\text{R}} \propto \begin{pmatrix} 0 & 0 & \sin(k_x) \\ 0 & 0 & \sin(k_y) \\ -\sin(k_x) & -\sin(k_y) & 0 \end{pmatrix}, \quad (\text{A1})$$

in the $t_{2g} = \{d_{yz}, d_{zx}, d_{xy}\}$ basis. However, this expression captures only the lowest-order in-plane processes and is not sufficient for a multi-layer slab geometry.

Following the approach of Ref. [40] and its multi-layer generalization in Ref. [19], we derive the full Rashba matrices including both NN and NNN processes.

For clarity, in the follow we adopt a first-quantization notation.

The derivation proceeds as follows. For a given orientation of the interfacial electric field, we first determine the linear-in-field correction to the local t_{2g} orbital wavefunctions. We then evaluate the corresponding matrix elements of the unperturbed tight-binding Hamiltonian in the three-dimensional Brillouin zone, obtaining an effective orbital Rashba Hamiltonian $H^{\text{R}}(\mathbf{K})$.

To construct the slab model, we split $\mathbf{K} = (\mathbf{k}, k_z)$ into in-plane momentum \mathbf{k} and the component k_z orthogonal

to the interface, and discretize the perpendicular direction. In this step, phase factors $e^{\pm ik_z}$ are identified with interlayer hoppings, allowing us to decompose H^{R} into in-plane and out-of-plane (interlayer) blocks.

a. (001) direction

For an electric field oriented along \hat{z} , the linear correction to the t_{2g} orbitals reads [40]

$$|d'_{yz}\rangle = \frac{\eta_p}{\sqrt{5}} |p_y\rangle, \quad (\text{A2})$$

$$|d'_{zx}\rangle = \frac{\eta_p}{\sqrt{5}} |p_x\rangle, \quad (\text{A3})$$

$$|d'_{xy}\rangle = 0. \quad (\text{A4})$$

Here η_p contains the radial matrix element induced by the electric field and its dependency by the electric potential $\varphi(z)$ as $\eta_p \sim \frac{\varphi(z)}{a' 10 \text{ eV/nm}}$, where a' being the distance between two adjacent layers.

Let H_0 denote the unperturbed Hamiltonian, i.e. the sum of Eqs. (1)–(5). To linear order in the field-induced correction of the orbital wavefunctions, the matrix elements in the $\{d_\alpha(\mathbf{K})\}$ basis are

$$\langle d_\alpha(\mathbf{K}) | H_0 | d_\beta(\mathbf{K}) \rangle = \sum_{\mathbf{R}, s=x,y,z} (c_{\alpha,s}^* \langle p_s | H_0 | d_\beta(-\mathbf{R}) \rangle + c_{\beta,s} \langle p_s | H_0 | d_\alpha(-\mathbf{R}) \rangle^*) e^{i\mathbf{K}\cdot\mathbf{R}}, \quad (\text{A5})$$

where α, β running over the orbital degrees of freedom and $c_{\alpha,s}$ are the coefficients defined in Eqs. (A2)–(A4).

For convenience, we introduce the Slater–Koster combinations

$$p_1 \equiv V_{pd\pi}, \quad p_3 \equiv -2V_{pd\pi} + \sqrt{3}V_{pd\sigma}, \quad (\text{A6})$$

where $V_{pd\pi}$ and $V_{pd\sigma}$ are the Slater–Koster $pd\pi$ and $pd\sigma$ overlap integrals [47].

a. *Nearest neighbors.* Restricting to NN $\mathbf{R} = \pm a_0 \hat{\xi}$, with $\hat{\xi} \in \{\hat{x}, \hat{y}, \hat{z}\}$, we obtain

$$H_a^{\text{R}} = p_1 \eta_p (\sqrt{2})^{7/2} \frac{2i}{\sqrt{5}} \begin{pmatrix} 0 & 0 & \sin(K_x) \\ 0 & 0 & \sin(K_y) \\ -\sin(K_x) & -\sin(K_y) & 0 \end{pmatrix}, \quad (\text{A7})$$

where \mathbf{K} is measured in units of a_0^{-1} . The factor $(\sqrt{2})^{7/2}$ accounts for the relative scaling between NN and NNN contributions. Equation (A7) corresponds to the standard orbital Rashba structure for the (001) orientation.

b. *Next-to-nearest neighbors.* For NNN $\mathbf{R} = \pm a_0(\hat{\xi} + \lambda\hat{\mu})$, with $\lambda = \pm 1$ and $\hat{\mu} = \hat{x}, \hat{y}, \hat{z}$ with $\hat{\mu} \neq \hat{\xi}$,

the matrix is

$$H_{\sqrt{2}a}^{\text{R}} = \eta_p \frac{4i}{\sqrt{5}} \begin{pmatrix} 0 & 0 & F_x(\mathbf{K}) \\ 0 & 0 & F_y(\mathbf{K}) \\ -F_x(\mathbf{K}) & -F_y(\mathbf{K}) & 0 \end{pmatrix}. \quad (\text{A8})$$

having defined

$$F_x(\mathbf{K}) = [(p_1 + p_3) \cos(K_y) + p_1 \cos(K_z)] \sin(K_x), \quad (\text{A9})$$

$$F_y(\mathbf{K}) = [(p_1 + p_3) \cos(K_x) + p_1 \cos(K_z)] \sin(K_y), \quad (\text{A10})$$

c. *Slab decomposition.* We now decompose $\mathbf{K} = (\mathbf{k}, K_z)$, where $\mathbf{k} = (k_x, k_y)$ is the in-plane momentum (here the redefinition is purely formally in order to unify the notation and remember that we switched to a 2D layered system). Upon discretization of the z direction, $e^{\pm iK_z}$ are identified with interlayer hoppings.

Since H_a^{R} does not depend on K_z , it contributes only to in-plane processes:

$$H_{a,\text{in-plane}}^{\text{R}}(\mathbf{k}) = p_1 \eta_p (\sqrt{2})^{7/2} \frac{2i}{\sqrt{5}} \begin{pmatrix} 0 & 0 & \sin(k_x) \\ 0 & 0 & \sin(k_y) \\ -\sin(k_x) & -\sin(k_y) & 0 \end{pmatrix}. \quad (\text{A11})$$

For the NNN contribution, using $\cos K_z = \frac{1}{2}(e^{iK_z} + e^{-iK_z})$, we separate in-plane and interlayer terms as

$$H_{\sqrt{2}a}^{\mathbf{R}}(\mathbf{K}) = H_{\sqrt{2}a,\text{in-plane}}^{\mathbf{R}}(\mathbf{k}) + e^{iK_z} H_{\sqrt{2}a,\text{out-of-plane}}^{\mathbf{R}}(\mathbf{k}) + e^{-iK_z} \left[H_{\sqrt{2}a,\text{out-of-plane}}^{\mathbf{R}}(\mathbf{k}) \right]^\dagger. \quad (\text{A12})$$

Dropping the $\cos(K_z)$ term yields the purely in-plane NNN matrix:

$$\tilde{F}_x(\mathbf{k}) = (p_1 + p_3) \cos(k_y) \sin(k_x), \quad (\text{A13})$$

$$\tilde{F}_y(\mathbf{k}) = (p_1 + p_3) \cos(k_x) \sin(k_y), \quad (\text{A14})$$

$$H_{\sqrt{2}a,\text{in-plane}}^{\mathbf{R}}(\mathbf{k}) = \eta_p \frac{4i}{\sqrt{5}} \begin{pmatrix} 0 & 0 & \tilde{F}_x(\mathbf{k}) \\ 0 & 0 & \tilde{F}_y(\mathbf{k}) \\ -\tilde{F}_x(\mathbf{k}) & -\tilde{F}_y(\mathbf{k}) & 0 \end{pmatrix}. \quad (\text{A15})$$

The remaining $\cos(K_z)$ contribution generates the interlayer hopping:

$$H_{\sqrt{2}a,\text{out-of-plane}}^{\mathbf{R}}(\mathbf{k}) = \eta_p \frac{4i}{\sqrt{5}} \frac{p_1}{2} \begin{pmatrix} 0 & 0 & \sin(k_x) \\ 0 & 0 & \sin(k_y) \\ -\sin(k_x) & -\sin(k_y) & 0 \end{pmatrix}. \quad (\text{A16})$$

b. (110) direction

For an electric field oriented along $(\hat{x} + \hat{y})/\sqrt{2}$, the linear corrections to the t_{2g} orbitals read

$$|d'_{yz}\rangle = \frac{\eta_p}{\sqrt{10}} |p_z\rangle, \quad (\text{A17})$$

$$|d'_{zx}\rangle = \frac{\eta_p}{\sqrt{10}} |p_z\rangle, \quad (\text{A18})$$

$$|d'_{xy}\rangle = \frac{\eta_p}{\sqrt{10}} (|p_x\rangle + |p_y\rangle). \quad (\text{A19})$$

We first evaluate the Rashba matrix elements in the cubic coordinate system (x, y, z) using Eq. (A5).

a. Nearest neighbors. For $\mathbf{R} = \pm a_0 \hat{\xi}$, we define

$$A(\mathbf{K}) = p_1 (\sin K_x - \sin K_y), \quad (\text{A20})$$

$$B(\mathbf{K}) = p_1 \sin K_z, \quad (\text{A21})$$

and obtain

$$H_a^{\mathbf{R}} = \frac{2i}{\sqrt{10}} (\sqrt{2})^{7/2} \begin{pmatrix} 0 & A(\mathbf{K}) & -B(\mathbf{K}) \\ -A(\mathbf{K}) & 0 & -B(\mathbf{K}) \\ B(\mathbf{K}) & B(\mathbf{K}) & 0 \end{pmatrix}. \quad (\text{A22})$$

b. Next-to-nearest neighbors. For $\mathbf{R} = \pm a_0 (\hat{\xi} + \lambda \hat{\mu})$, with $\lambda = \pm 1$ and $\hat{\mu} \neq \hat{\xi}$, we introduce

$$C(\mathbf{K}) = 2 \left[p_1 \cos\left(\frac{K_x - K_y}{2}\right) + (p_1 + p_3) \cos\left(\frac{K_x + K_y}{2}\right) \cos K_z \right] \sin\left(\frac{K_x - K_y}{2}\right), \quad (\text{A23})$$

$$D(\mathbf{K}) = \left[p_1 \cos K_x + (p_1 + p_3) \cos K_y \right] \sin K_z, \quad (\text{A24})$$

$$\bar{D}(\mathbf{K}) = \left[(p_1 + p_3) \cos K_x + p_1 \cos K_y \right] \sin K_z. \quad (\text{A25})$$

The corresponding matrix reads

$$H_{\sqrt{2}a}^{\mathbf{R}}(\mathbf{K}) = \frac{4i}{\sqrt{10}} \begin{pmatrix} 0 & C(\mathbf{K}) & -D(\mathbf{K}) \\ -C(\mathbf{K}) & 0 & -\bar{D}(\mathbf{K}) \\ D(\mathbf{K}) & \bar{D}(\mathbf{K}) & 0 \end{pmatrix}. \quad (\text{A26})$$

c. Rotation to the (110) slab coordinates. We now express the result in the orthonormal basis

$$\hat{\mathbf{e}}_1 = \frac{1}{\sqrt{2}}(1, -1, 0), \quad \hat{\mathbf{e}}_2 = (0, 0, 1), \quad \hat{\mathbf{e}}_3 = \frac{1}{\sqrt{2}}(1, 1, 0), \quad (\text{A27})$$

where $\hat{\mathbf{e}}_3$ is normal to the interface.

The crystal momentum transforms as

$$K_x = \frac{k_z + k_y}{\sqrt{2}}, \quad K_y = \frac{k_z - k_y}{\sqrt{2}}, \quad K_z = k_x, \quad (\text{A28})$$

where $\mathbf{k} = (k_x, k_y)$ is the in-plane momentum of the slab.

$$H_{\sqrt{2}a}^{\text{R}}(\mathbf{K}) = H_{\sqrt{2}a, \text{in-plane}}^{\text{R}}(\mathbf{k}) + e^{ik_z/\sqrt{2}} H_{\sqrt{2}a, \text{out-of-plane}}^{\text{R}}(\mathbf{k}) + e^{-ik_z/\sqrt{2}} \left[H_{\sqrt{2}a, \text{out-of-plane}}^{\text{R}}(\mathbf{k}) \right]^\dagger. \quad (\text{A29})$$

The total in-plane Rashba block is

$$H_{\text{in-plane}}^{\text{R}}(\mathbf{k}) = \eta_p p_1 \frac{2i}{\sqrt{10}} \begin{pmatrix} 0 & a(\mathbf{k}) & -b(\mathbf{k}) \\ -a(\mathbf{k}) & 0 & -b(\mathbf{k}) \\ b(\mathbf{k}) & b(\mathbf{k}) & 0 \end{pmatrix}, \quad (\text{A30})$$

where

$$a(\mathbf{k}) = 2 \sin(\sqrt{2} k_y), \quad (\text{A31})$$

$$b(\mathbf{k}) = (\sqrt{2})^{7/2} \sin(k_x). \quad (\text{A32})$$

The interlayer Rashba hopping reads

$$H_{\sqrt{2}a, \text{out-of-plane}}^{\text{R}}(\mathbf{k}) = \frac{2i}{\sqrt{10}} \begin{pmatrix} 0 & \sin\left(\frac{k_y}{\sqrt{2}}\right) u(\mathbf{k}) & -\sin(k_x) v(\mathbf{k}) \\ -\sin\left(\frac{k_y}{\sqrt{2}}\right) u(\mathbf{k}) & 0 & -\sin(k_x) v^*(\mathbf{k}) \\ \sin(k_x) v(\mathbf{k}) & \sin(k_x) v^*(\mathbf{k}) & 0 \end{pmatrix}, \quad (\text{A33})$$

with

$$u(\mathbf{k}) = (\sqrt{2})^{7/2} p_1 + 2(p_1 + p_3) \cos(k_x), \quad (\text{A34})$$

$$v(\mathbf{k}) = (2p_1 + p_3) \cos\left(\frac{k_y}{\sqrt{2}}\right) - i p_3 \sin\left(\frac{k_y}{\sqrt{2}}\right). \quad (\text{A35})$$

c. (111) direction

For an electric field oriented along the (111) direction, the linear corrections to the t_{2g} orbitals read

$$|d'_{xy}\rangle = \frac{\eta_p}{\sqrt{15}} (|p_x\rangle + |p_y\rangle), \quad (\text{A36})$$

$$|d'_{yz}\rangle = \frac{\eta_p}{\sqrt{15}} (|p_y\rangle + |p_z\rangle), \quad (\text{A37})$$

$$|d'_{zx}\rangle = \frac{\eta_p}{\sqrt{15}} (|p_z\rangle + |p_x\rangle). \quad (\text{A38})$$

The Rashba matrices for the (111) orientation were previously derived for a bilayer geometry in Refs. [19, 20], using a different gauge convention. Here we adopt a gauge consistent with the present slab formulation and

Upon discretization of the perpendicular direction, the factors $e^{\pm ik_z/\sqrt{2}}$ correspond to hoppings between adjacent layers.

d. *Slab decomposition.* The NN contribution does not generate interlayer hoppings and therefore enters only the in-plane block.

The NNN term produces both in-plane and interlayer processes, which we decompose as

extend the construction to an arbitrary number of layers. The matrices reported below are therefore obtained by an appropriate regauging of those in Refs. [19, 20] and by generalizing the bilayer construction to the multilayer case, including NNN processes coupling layers separated by two lattice spacings.

a. *Coordinate system.* We introduce the orthonormal basis

$$\begin{cases} \hat{\mathbf{e}}_1 = \frac{1}{\sqrt{2}}(1, -1, 0), \\ \hat{\mathbf{e}}_2 = \frac{1}{\sqrt{6}}(1, 1, -2), \\ \hat{\mathbf{e}}_3 = \frac{1}{\sqrt{3}}(1, 1, 1). \end{cases} \quad (\text{A39})$$

where $\hat{\mathbf{e}}_3$ is normal to the interface and $(\hat{\mathbf{e}}_1, \hat{\mathbf{e}}_2)$ span the (111) plane.

The lattice vector decomposes as

$$\mathbf{R} = u_1 \hat{\mathbf{e}}_1 + u_2 \hat{\mathbf{e}}_2 + u_3 \hat{\mathbf{e}}_3. \quad (\text{A40})$$

The in-plane Ta-Ta distance is

$$\tilde{a} = \sqrt{\frac{2}{3}} a_0, \quad (\text{A41})$$

while the interlayer spacing along $\hat{\mathbf{e}}_3$ is

$$\tilde{a}' = \frac{a_0}{\sqrt{3}}. \quad (\text{A42})$$

In the following, the in-plane momentum $\mathbf{k} = (k_x, k_y)$ denotes the components along $(\hat{\mathbf{e}}_1, \hat{\mathbf{e}}_2)$ and is expressed in units of \tilde{a}^{-1} . The perpendicular component k_z is measured in units of $(\tilde{a}')^{-1}$.

b. *In-plane Rashba coupling.* Defining

$$s_i(\mathbf{k}) = \sin \kappa_i(\mathbf{k}) \quad (\text{A43})$$

with

$$\begin{cases} \kappa_1 = -\frac{\sqrt{3}}{2} k_x + \frac{3}{2} k_y, \\ \kappa_2 = -\frac{\sqrt{3}}{2} k_x - \frac{3}{2} k_y, \\ \kappa_3 = \sqrt{3} k_x. \end{cases} \quad (\text{A44})$$

the intra-layer Rashba Hamiltonian takes the form

$$H_{\sqrt{2}a,\text{in-plane}}^{\text{R}}(\mathbf{k}) = H_{\pi}(\mathbf{k}) + H_{\sigma}(\mathbf{k}), \quad (\text{A45})$$

with

$$H_{\pi}(\mathbf{k}) = \eta_p \frac{2i}{\sqrt{15}} p_1 \begin{pmatrix} 0 & \alpha_{12} & \alpha_{13} \\ -\alpha_{12} & 0 & \alpha_{23} \\ -\alpha_{13} & -\alpha_{23} & 0 \end{pmatrix}, \quad (\text{A46})$$

$$H_{\sigma}(\mathbf{k}) = \eta_p \frac{2i}{\sqrt{15}} (2p_1 + p_3) \begin{pmatrix} 0 & \beta_{12} & \beta_{13} \\ -\beta_{12} & 0 & \beta_{23} \\ -\beta_{13} & -\beta_{23} & 0 \end{pmatrix}, \quad (\text{A47})$$

where

$$\alpha_{12} = -2s_1 + s_2 + s_3, \quad \beta_{12} = -s_2 - s_3, \quad (\text{A48})$$

$$\alpha_{13} = -2s_3 + s_1 - s_2, \quad \beta_{13} = -s_1 + s_2, \quad (\text{A49})$$

$$\alpha_{23} = 2s_2 - s_1 + s_3, \quad \beta_{23} = s_1 - s_3. \quad (\text{A50})$$

In contrast to the (001) and (110) cases, the purely in-plane Rashba coupling for the (111) geometry originates entirely from NNN processes.

c. Slab decomposition. In the slab geometry, the full Rashba Hamiltonian can be written as

$$H^{\text{R}}(\mathbf{K}) = H_{\sqrt{2}a,\text{in-plane}}^{\text{R}}(\mathbf{k}) + e^{ik_z} H_{a,\text{out-of-plane}}^{\text{R}}(\mathbf{k}) + e^{-ik_z} H_{a,\text{out-of-plane}}^{\text{R}\dagger}(\mathbf{k}) + e^{i2k_z} H_{\sqrt{2}a,\text{out-of-plane}}^{\text{R}}(\mathbf{k}) + e^{-i2k_z} H_{\sqrt{2}a,\text{out-of-plane}}^{\text{R}\dagger}(\mathbf{k}). \quad (\text{A51})$$

Here the NN term connects adjacent layers, while the NNN term couples layers separated by two lattice spacings.

d. Interlayer hopping (nearest neighbors). In the present gauge, the corresponding matrix reads

$$H_{a,\text{out-of-plane}}^{\text{R}}(\mathbf{k}) = \eta_p \frac{p_1}{\sqrt{15}} (\sqrt{2})^{7/2} \begin{pmatrix} 0 & h_{12}(\mathbf{k}) & h_{13}(\mathbf{k}) \\ -h_{12}(\mathbf{k}) & 0 & h_{23}(\mathbf{k}) \\ -h_{13}(\mathbf{k}) & -h_{23}(\mathbf{k}) & 0 \end{pmatrix}, \quad (\text{A52})$$

with

$$h_{12}(\mathbf{k}) = -2i e^{-\frac{i}{2}k_y} \sin\left(\frac{\sqrt{3}}{2}k_x\right), \quad (\text{A53})$$

$$h_{13}(\mathbf{k}) = -e^{ik_y} + e^{-\frac{i}{2}(\sqrt{3}k_x + k_y)}, \quad (\text{A54})$$

$$h_{23}(\mathbf{k}) = -e^{ik_y} + e^{\frac{i}{2}(\sqrt{3}k_x - k_y)}. \quad (\text{A55})$$

e. Interlayer hopping (next-to-nearest neighbors). Because of the triangular stacking of the (111) planes, NNN Slater–Koster processes generate additional Rashba terms connecting layers separated by two lattice spacings. These contributions are essential in a multilayer geometry, where they provide the leading correction beyond the bilayer model. The corresponding matrix is

$$H_{\sqrt{2}a,\text{out-of-plane}}^{\text{R}}(\mathbf{k}) = \frac{\eta_p}{\sqrt{15}} (p_1 + p_3) \begin{pmatrix} 0 & g_{12}(\mathbf{k}) & g_{13}(\mathbf{k}) \\ -g_{12}(\mathbf{k}) & 0 & g_{23}(\mathbf{k}) \\ -g_{13}(\mathbf{k}) & -g_{23}(\mathbf{k}) & 0 \end{pmatrix}, \quad (\text{A56})$$

where

$$g_{12}(\mathbf{k}) = -\frac{1}{2} e^{\frac{i}{2}k_y} \sin\left(\frac{\sqrt{3}}{2}k_x\right), \quad (\text{A57})$$

$$g_{13}(\mathbf{k}) = -\frac{1}{4i} \left[-e^{-ik_y} + e^{\frac{i}{2}(\sqrt{3}k_x + k_y)} \right], \quad (\text{A58})$$

$$g_{23}(\mathbf{k}) = \frac{1}{2} e^{-\frac{i}{4}(\sqrt{3}k_x + k_y)} \sin\left(\frac{1}{4}(\sqrt{3}k_x - 3k_y)\right). \quad (\text{A59})$$

Appendix B: Dielectric function

In this Appendix we describe the fitting procedure adopted for the dielectric function $\varepsilon(F)$ entering Eqs. (6). As discussed in the main text, we assume $\varepsilon(F)$ to be independent of both the crystallographic direction and the 2DEG density. Within this approximation, the screening properties at the interface are taken to be the same as in the bulk.

We adopt the following ansatz for the dielectric function:

$$\varepsilon(F) = 1 + \frac{\chi_0}{\left(1 + \frac{F^2}{F_C^2}\right)^\gamma}, \quad (\text{B1})$$

which reproduces the low-temperature antiferroelectric response of KTO. The parameters F_C , χ_0 , and γ are determined through a fitting procedure. To reduce the number of free parameters, we restrict γ to the values $\gamma = 1/3$ and $2/5$, as commonly assumed in the literature [21, 41, 48, 49].

We define a benchmark electronic band structure for the (111) interface to be fitted against the ARPES data of Ref. [15]. In Ref. [18], the band structure was reproduced using an effective potential ramp of the form

$$\varphi_{\text{eff}}(z) = \beta \left(1 - e^{-z\frac{\alpha}{\beta}}\right), \quad (\text{B2})$$

with $\alpha = 0.4$ V, $\beta = 0.97$ V, and z the dimensionless layer index. This potential saturates for $z \rightarrow \infty$ and

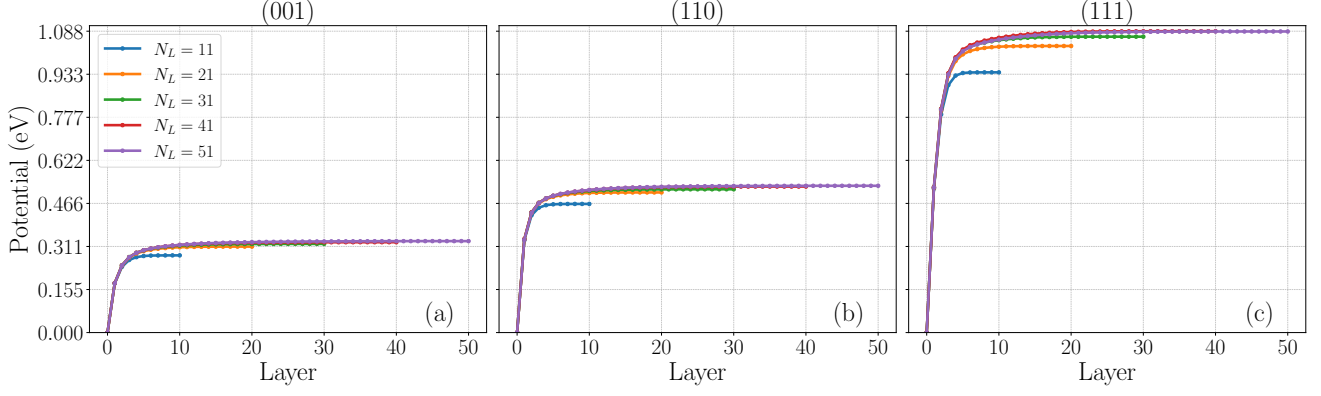


Figure 8. Electrostatic potential φ as a function of the layer index for different slab thicknesses N_L at $n_{2D} = 1.6 \times 10^{14} \text{ cm}^{-2}$: (a) (001), (b) (110), and (c) (111) orientations.

provides a good description of the experimental bands for $\mu = 0.15 \text{ eV}$ above the band bottom.

Since the agreement between the confined band structure obtained with φ_{eff} and the experimental data is satisfactory in the first few layers, we proceed as follows:

- We compute the electronic density profile n_z^{Th} over a 40-layer slab using Eq. (B2) with $\mu = 0.15 \text{ eV}$, corresponding to a total sheet density $n_{2D} = 1.6 \times 10^{14} \text{ cm}^{-2}$.
- We determine the electric displacement

$$D_z = |e| \left(\sum_{i=1}^{40} n_i^{\text{Th}} - \sum_{i=1}^z n_i^{\text{Th}} \right).$$

- For a given choice of $\varepsilon(F)$, we obtain the electric field F_z by solving

$$D_z = \varepsilon_0 \varepsilon(F_z) F_z.$$

- We compute the reference electric field associated with the effective potential,

$$F_z^{\text{Th}} = \frac{1}{\tilde{a}'} \partial_z \varphi_{\text{eff}} = \frac{\alpha}{\tilde{a}'} e^{-z \frac{\alpha}{\tilde{a}'}} ,$$

where $\tilde{a}' = 3.988/\sqrt{3} \text{ \AA}$ is the interlayer distance between Ta layers in the (111) direction.

- We evaluate

$$\chi^2 = \sum_{l=1}^M \frac{(F_l^{\text{Th}} - F_l)^2}{M(F_l^{\text{Th}})^2}$$

as a measure of the agreement between the two electric fields.

- Finally, we minimize χ^2 with respect to F_C , χ_0 , and γ , restricting the fit to the first $M = 4$ layers. This choice reflects the fact that φ_{eff} was optimized to reproduce the 2DEG bands near the interface, while its behavior deeper in the slab is less reliable.

The optimal parameters are $\gamma = 1/3$, $\chi_0 = 3600$, and $F_C = 443,7 \text{ kV/m}$, consistent with the typical order of magnitude reported for related oxides [21].

Appendix C: Bulk limit

In this Appendix we analyze the convergence of the electrostatic potential as a function of the total number of layers N_L . The goal is to verify that the slab is sufficiently thick to reproduce the bulk limit when the layer index approaches the boundary, $N_z \rightarrow N_L$.

Figure 8 shows the electrostatic potential profile obtained for different slab thicknesses at fixed sheet density $n_{2D} = 1.6 \times 10^{14} \text{ cm}^{-2}$. Convergence to the bulk behavior is achieved for $N_L \gtrsim 41$. Accordingly, in all calculations presented in this work we set $N_L = 51$.

Appendix D: Mean field treatment of superconductivity

In this Appendix we provide details on the theoretical description of inhomogeneous superconductivity.

We start from a generic (screened) two-body interaction in real space

$$H_{\text{int}} = \frac{1}{2} \sum_{\sigma\sigma'} \int d^3r d^3r' \psi_{\sigma}^{\dagger}(\mathbf{r}) \psi_{\sigma'}^{\dagger}(\mathbf{r}') U(\mathbf{r}-\mathbf{r}') \psi_{\sigma'}(\mathbf{r}') \psi_{\sigma}(\mathbf{r}), \quad (\text{D1})$$

and expand the field operators in a localized (Wannier-like) orbital basis,

$$\psi_{\sigma}(\mathbf{r}) = \sum_{\mathbf{R}, \alpha} \varphi_{\alpha}(\mathbf{r} - \mathbf{R}) c_{\mathbf{R}\alpha\sigma}, \quad (\text{D2})$$

where \mathbf{R} labels lattice sites and α denotes local orbital degrees of freedom.

Retaining only the dominant on-site, intra-orbital contribution yields the effective local interaction

$$H_{\text{int}} \simeq -U_{\text{eff}} \sum_{\mathbf{R}, \alpha} c_{\mathbf{R}\alpha\uparrow}^\dagger c_{\mathbf{R}\alpha\downarrow}^\dagger c_{\mathbf{R}\alpha\downarrow} c_{\mathbf{R}\alpha\uparrow}, \quad (\text{D3})$$

with

$$U_{\text{eff}} = \int d^3r d^3r' |\varphi_\alpha(\mathbf{r})|^2 U(\mathbf{r} - \mathbf{r}') |\varphi_\alpha(\mathbf{r}')|^2. \quad (\text{D4})$$

$$-U c_{\mathbf{R}\alpha\uparrow}^\dagger c_{\mathbf{R}\alpha\downarrow}^\dagger c_{\mathbf{R}\alpha\downarrow} c_{\mathbf{R}\alpha\uparrow} \rightarrow -U \left(\Delta_{\mathbf{R}}^* c_{\mathbf{R}\alpha\downarrow} c_{\mathbf{R}\alpha\uparrow} + \Delta_{\mathbf{R}} c_{\mathbf{R}\alpha\uparrow}^\dagger c_{\mathbf{R}\alpha\downarrow}^\dagger \right) + U |\Delta_{\mathbf{R}}|^2, \quad (\text{D5})$$

where

$$\Delta_{\mathbf{R}} = \langle c_{\mathbf{R}\alpha\downarrow} c_{\mathbf{R}\alpha\uparrow} \rangle, \quad (\text{D6})$$

and we assume the same order parameter for all orbitals.

Slab geometry and layer-resolved formulation

We now consider slab geometries, where translational invariance is preserved only in the plane. We decompose $\mathbf{R} = (\mathbf{r}, z)$, with \mathbf{r} the in-plane coordinate and z the discrete layer index.

The superconducting order parameter becomes layer-resolved,

$$\Delta_z = \langle c_{\mathbf{r}z\alpha\downarrow} c_{\mathbf{r}z\alpha\uparrow} \rangle, \quad (\text{D7})$$

while remaining uniform in-plane.

We introduce the partial Fourier transform

$$c_{\mathbf{r}z\alpha\sigma} = \frac{1}{\sqrt{\mathcal{A}}} \sum_{\mathbf{k}} e^{i\mathbf{k}\cdot\mathbf{r}} c_{\mathbf{k}z\alpha\sigma}, \quad \sum_{\mathbf{k}} = \mathcal{A} \int \frac{d^2k}{(2\pi)^2}, \quad (\text{D8})$$

where \mathcal{A} is the in-plane area.

With these conventions, the mean-field pairing term reads

$$H_{\text{int}} = -U \sum_{\mathbf{k}>0, z, \alpha} (\Delta_z^* c_{\mathbf{k}z\alpha\uparrow} c_{-\mathbf{k}z\alpha\downarrow} + \text{h.c.}) + 3U\mathcal{A} \sum_z |\Delta_z|^2. \quad (\text{D9})$$

Diagonalizing the full BdG Hamiltonian in particle-hole basis, we obtain

$$H = \sum_{\mathbf{k}>0, n} \lambda_{\mathbf{k}n} \left(\Gamma_{\mathbf{k}n}^\dagger \Gamma_{\mathbf{k}n} + \tilde{\Gamma}_{\mathbf{k}n}^\dagger \tilde{\Gamma}_{\mathbf{k}n} \right) + 3U\mathcal{A} \sum_z |\Delta_z|^2, \quad (\text{D10})$$

where $\lambda_{\mathbf{k}n} \geq 0$, up to constants. Here $\Gamma_{\mathbf{k}n}$ and $\tilde{\Gamma}_{\mathbf{k}n}$ correspond to the positive- and negative-energy BdG branches, respectively, and are related by particle-hole symmetry.

The effective coupling U_{eff} has dimensions of energy and depends only on the microscopic interaction and on the localized orbital wavefunctions. In the following we denote it simply by U . Since the system changes when varying the crystallographic orientation, we adopt the same microscopic convention for U in all geometries.

Assuming local spin-singlet pairing, the interaction is decoupled at the mean-field level as

The free energy is therefore

$$F = -\frac{1}{\beta} \sum_{\mathbf{k}>0, n} \log[2 + 2 \cosh(\beta \lambda_{\mathbf{k}n})] + 3U\mathcal{A} \sum_z |\Delta_z|^2, \quad (\text{D11})$$

with $\beta = 1/(k_B T)$.

It is convenient to rescale $F \rightarrow F/\mathcal{A}$ and convert the momentum sum into an integral,

$$F = 3U \sum_z |\Delta_z|^2 - \frac{\mathcal{P}}{\beta} \sum_n \int d^2\mathbf{k} \log[2 + 2 \cosh(\beta \lambda_{\mathbf{k}n})], \quad (\text{D12})$$

where \mathcal{P} includes the in-plane unit-cell area, the Jacobian associated with the chosen coordinates, a factor 1/2 from restricting to $\mathbf{k} > 0$, and the momentum-space density of states.

For the three crystallographic orientations we obtain

$$\begin{cases} \mathcal{P}_{001} = \frac{1}{4\pi^2}, \\ \mathcal{P}_{110} = \frac{\sqrt{2}}{4\pi^2}, \\ \mathcal{P}_{111} = \frac{27}{8\pi^2}. \end{cases} \quad (\text{D13})$$

For the (111) orientation we use normal coordinates (ℓ_x, ℓ_y) defined by

$$k_x = \frac{\sqrt{3}}{2} \ell_x, \quad k_y = \ell_y - \frac{\ell_x}{2}. \quad (\text{D14})$$

Appendix E: Impact of confinement of superconductivity

For both the retarded and the instantaneous pairing mechanisms discussed in the main text, we minimized Eqs. (21) and (23). In this Appendix we present benchmark results for $\tilde{U}(z_0)$ and $U(z_0)$ in the two cases, together with the self-consistent values of z_0 obtained for the instantaneous interaction, as mentioned in the main text. This analysis allows us to further comment on the

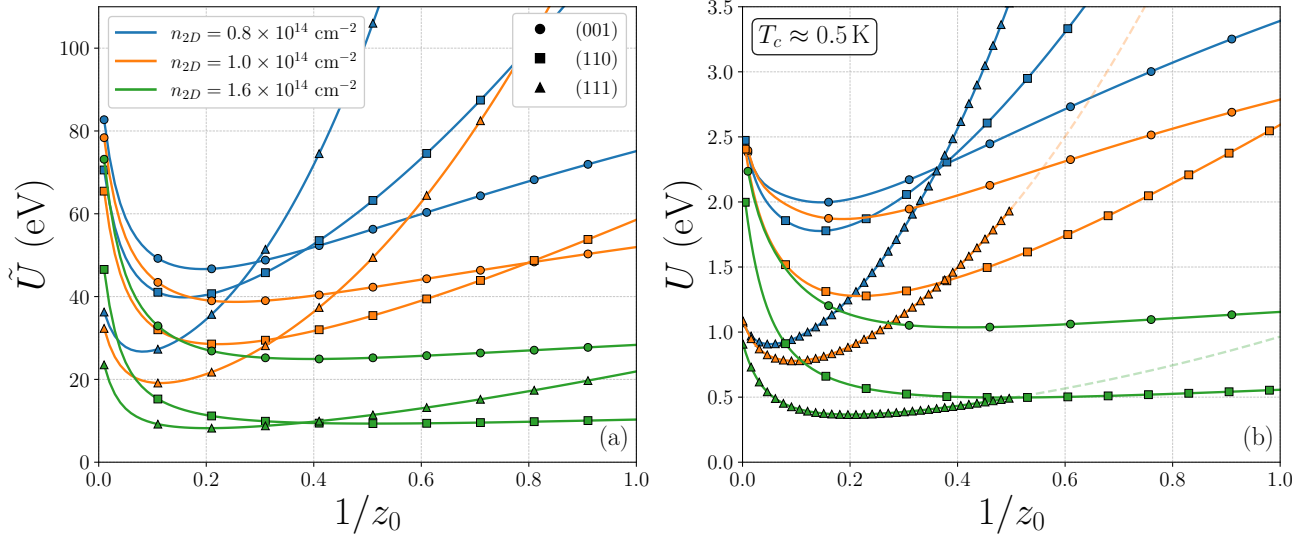


Figure 9. (a) Exponential factor \tilde{U} as a function of $1/z_0$. The limit $1/z_0 = 0$ corresponds to purely homogeneous superconductivity. (b) Superconducting coupling strength U as a function of $1/z_0$ for a benchmark $T_c \approx 0.5 \text{ K}$. For the (111) direction, dashed lines are fitted curves used only to interpolate missing points and guide the eye. In both panels, circles denote (001), squares (110), and triangles (111) directions, while colors correspond to different n_{2D} .

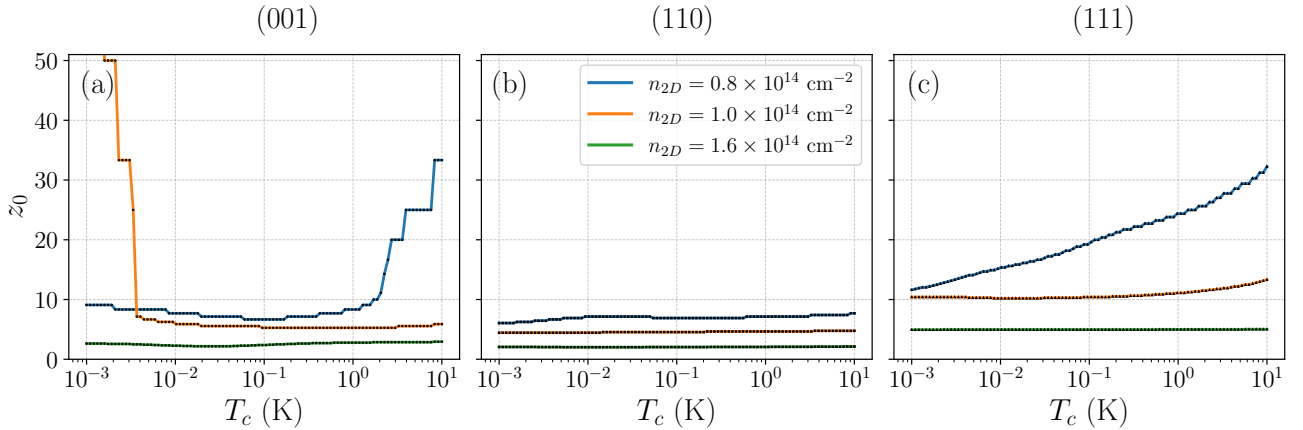


Figure 10. Superconducting penetration length z_0 as a function of the imposed critical temperature T_c for (a) (001), (b) (110), and (c) (111) directions, and for different benchmark values of n_{2D} .

assumption of homogeneous pairing and on the necessity of going beyond this limitation.

In Fig. 9 we show the exponential factor \tilde{U} as a function of $1/z_0$ for the phonon-mediated pairing mechanism, and the superconducting coupling strength U as a function of $1/z_0$ for a fixed benchmark critical temperature $T_c \approx 0.5 \text{ K}$ in the instantaneous case. In both cases we observe pronounced minima at finite values of $1/z_0$, corresponding to a preferred inhomogeneous solution. Interestingly, if one enforces a homogeneous solution in the instantaneous pairing mechanism, the values of U required to obtain $T_c \approx 0.5 \text{ K}$ are almost independent of n_{2D} . This indicates that the dominant contribution to superconductivity would not originate from the 2DEG, but rather from bulk states, an assumption that is physically implausible in the present context.

We now comment on the spatial extension of the superconducting order parameter across the slab. In the phonon-mediated case (see Fig. 6), there is a direct correlation between the spatial extension of the 2DEG and z_0 , since most of the LDOS at the Fermi level is localized within the 2DEG region.

For the instantaneous pairing mechanism, the superconducting penetration length z_0 at which the instability occurs depends explicitly on the chosen critical temperature. In Fig. 10 we show the evolution of z_0 as a function of the imposed T_c . The behavior is non-trivial. In particular, for the (001) direction there are regimes in which the most favorable solution corresponds to superconductivity extending throughout the entire slab. This behavior also depends on the carrier density.

Such non-trivial trends originate from the structure

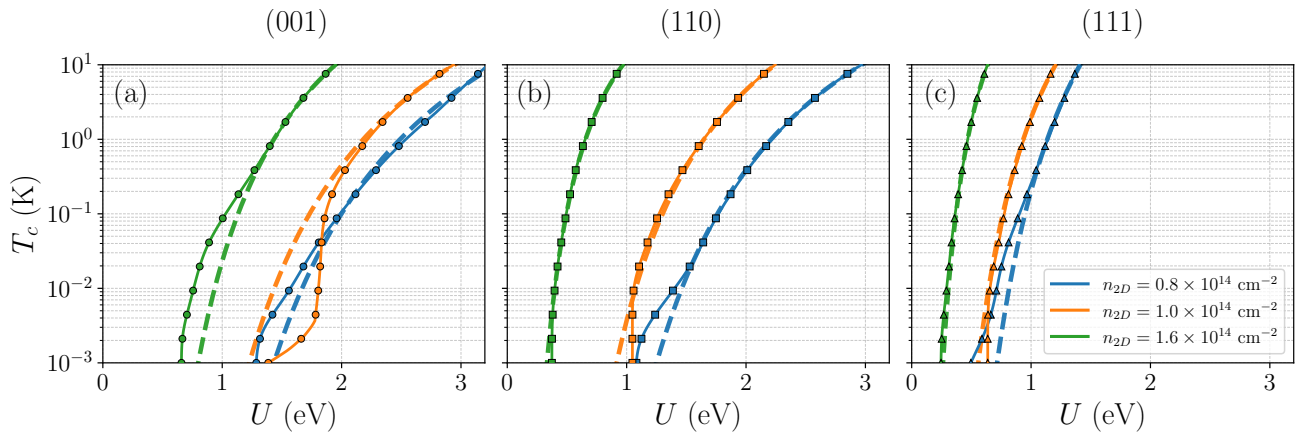


Figure 11. Critical temperature T_C for (a) (001), (b) (110), and (c) (111) directions, evaluated within the instantaneous interaction mechanism (solid lines and markers). The dashed lines correspond to an exponential fit $T_C \sim \omega_i \exp(-\tilde{U}/2U)$, where \tilde{U} is obtained self-consistently from the phonon-mediated pairing framework and ω_i is used as a fitting parameter in the large- U regime.

of the available 2DEG states. Reaching an instability at a given T_C requires either a sufficient density of states near the interface or a stronger attractive pairing interaction. Alternatively, the instability can be supported by involving bulk states farther from the interface.

For (111) direction at low density, the increase of z_0 with T_C shows the necessity of involving bulk states, whereas at higher density the electronic states localized near the interface are sufficient to sustain superconductivity without a significant extension into the bulk. The (110) direction, on the other hand, appears to be the most confined case, as it consistently involves contributions from folded bands at the Brillouin-zone boundary, predominantly localized in the first layer, where the LDOS exhibits a pronounced peak.

The analysis above clarifies how the instability optimizes its spatial profile through the self-consistent determination of z_0 . Having established this point, we now turn to the resulting dependence of the critical temperature on the pairing strength.

As pointed out in the main text, the difference between the predicted critical temperatures stems from the distinct functional dependence of the instability condition on the pairing strength in the two mechanisms. While in the phonon-mediated case the transition temperature follows a purely exponential BCS-like form, in

the instantaneous interaction the dependence of T_C on U deviates from a simple exponential at small coupling. This deviation is directly linked to the self-consistent determination of the optimal penetration length z_0 , which modifies the effective phase space available for pairing.

In Fig. 11 we make this comparison explicit. We plot the critical temperature obtained within the instantaneous mechanism as a function of U , and compare it with an exponential form $T_C \sim \omega_i \exp(-\tilde{U}/2U)$, where \tilde{U} is taken from the phonon-mediated framework and ω_i is used as a fitting parameter in the large- U regime.

For sufficiently large interaction strengths, all orientations recover an exponential dependence, demonstrating that the two mechanisms share the same asymptotic structure once the optimal spatial profile is selected. The remaining differences between (001), (110), and (111) interfaces are encoded in the prefactors, which are entirely determined by the normal-state electronic structure and the corresponding distribution of low-energy states across the slab.

At small U , however, deviations from the exponential behavior become evident, particularly for the (001) orientation, where a threshold-like onset of superconductivity appears. This confirms that the interplay between confinement, density of states, and spatial extension of the order parameter plays a crucial role in shaping the instability at weak coupling.

-
- [1] A. Ohtomo and H. Hwang, A high-mobility electron gas at the LaAlO₃/SrTiO₃ heterointerface, *Nature* **427**, 423 (2004).
 [2] A. Caviglia, S. Gariglio, N. Reyren, D. Jaccard, T. Schneider, M. Gabay, S. Thiel, G. Hammerl, J. Mannhart, and J.-M. Triscone, Electric field control of the LaAlO₃/SrTiO₃ interface ground state, *Nature*

456, 624 (2008).

- [3] A. D. Caviglia, M. Gabay, S. Gariglio, N. Reyren, C. Cancellieri, and J.-M. Triscone, Tunable rashba spin-orbit interaction at oxide interfaces, *Phys. Rev. Lett.* **104**, 126803 (2010).
 [4] S. Gariglio, A. Caviglia, J.-M. Triscone, and M. Gabay, A spin-orbit playground: Surfaces and interfaces of tran-

- sition metal oxides, *Reports on Progress in Physics* **82**, 012501 (2018).
- [5] A. Barthelemy, N. Bergeal, M. Bibes, A. Caviglia, R. Citro, M. Cuoco, A. Kalaboukhov, B. Kalisky, C. A. Perroni, J. Santamaria, D. Stornaiuolo, and M. Salluzzo, Quasi-two-dimensional electron gas at the oxide interfaces for topological quantum physics, *Europhysics Letters* **133**, 17001 (2021).
 - [6] A. Maiellaro, J. Settino, C. Guarcello, F. Romeo, and R. Citro, Hallmarks of orbital-flavored Majorana states in Josephson junctions based on oxide nanochannels, *Physical Review B* **107**, L201405 (2023).
 - [7] C. Guarcello, A. Maiellaro, J. Settino, I. Gaiardoni, M. Trama, F. Romeo, and R. Citro, Probing Topological Superconductivity of oxide nanojunctions using fractional Shapiro steps, *Chaos, Solitons & Fractals* **189**, 115596 (2024).
 - [8] A. Maiellaro, F. Romeo, M. Trama, I. Gaiardoni, J. Settino, C. Guarcello, N. Bergeal, M. Bibes, and R. Citro, Theory of charge-to-spin conversion under quantum confinement, *Phys. Rev. Res.* **7**, 043100 (2025).
 - [9] A. Maiellaro, F. Romeo, M. Trama, J. Settino, C. Guarcello, C. A. Perroni, P. Wójcik, B. Szafran, D. Stornaiuolo, M. Salluzzo, *et al.*, Spin Hall and Edelstein effects in a ballistic quantum dot with Rashba spin-orbit coupling, *arXiv preprint arXiv:2602.02036* (2026).
 - [10] I. Gaiardoni, M. Trama, A. Maiellaro, C. Guarcello, F. Romeo, and R. Citro, Boltzmann theory of the inverse Edelstein effect in a two-dimensional Rashba gas, *arXiv preprint arXiv:2601.02473* (2026).
 - [11] C. Liu, X. Yan, D. Jin, Y. Ma, H.-W. Hsiao, Y. Lin, T. M. Bretz-Sullivan, X. Zhou, J. Pearson, B. Fisher, D. Fong, H. Zhou, and A. Bhattacharya, Two-Dimensional Superconductivity and Anisotropic Transport at KTaO_3 (111) Interfaces, *Science* **371**, 716 (2021).
 - [12] X. Hua, F. Meng, Z. Huang, Z. Li, S. Wang, B. Ge, Z. Xiang, and X. Chen, Tunable two-dimensional superconductivity and spin-orbit coupling at the EuO/KTaO_3 (110) interface, *npj Quantum Materials* **7**, 97 (2022).
 - [13] E. G. Arnault, A. H. Al-Tawhid, S. Salmani-Rezaie, D. A. Muller, D. P. Kumah, M. S. Bahramy, G. Finkelstein, and K. Ahadi, Anisotropic Superconductivity at KTaO_3 (111) Interfaces, *Science Advances* **9**, eadf1414 (2023).
 - [14] S. Mallik, B. Göbel, H. Witt, L. M. Vicente-Arche, S. Varotto, J. Bréhin, G. Ménard, D. Tamsaout, A. F. Santander-Syro, F. Fortuna, F. Bertran, P. Le Fèvre, J. Rault, I. Boventer, I. Mertig, A. Barthélémy, N. Bergeal, and M. Bibes, Electronic Band Structure of Superconducting KTaO_3 (111) Interfaces, *APL Materials* **11**, 121108 (2023).
 - [15] F. Y. Bruno, S. McKeown Walker, S. Riccò, A. de la Torre, Z. Wang, A. Tamai, T. K. Kim, M. Hoesch, M. S. Bahramy, and F. Baumberger, Band Structure and Spin-Orbital Texture of the (111)- KTaO_3 2D Electron Gas, *Advanced Electronic Materials* **5**, 1800860 (2019).
 - [16] Y. Chen, M. d'Antuono, M. Trama, D. Preziosi, B. Jouault, F. Teppe, C. Consejo, C. A. Perroni, R. Citro, D. Stornaiuolo, *et al.*, Dirac-Like Fermions Anomalous Magneto-Transport in a Spin-Polarized Oxide 2D Electron System, *Advanced Materials* **37**, 2410354 (2025).
 - [17] A. H. Al-Tawhid, R. Sun, A. H. Comstock, D. P. Kumah, D. Sun, and K. Ahadi, Spin-to-charge conversion at KTaO_3 (111) interfaces, *Applied Physics Letters* **126**, 025101 (2025).
 - [18] J. Zhai, M. Trama, H. Liu, Z. Zhu, Y. Zhu, C. A. Perroni, R. Citro, P. He, and J. Shen, Large Nonlinear Transverse Conductivity and Berry Curvature in KTaO_3 Based Two-Dimensional Electron Gas, *Nano Letters* **23**, 11892 (2023).
 - [19] M. Trama, V. Cataudella, C. A. Perroni, F. Romeo, and R. Citro, Gate tunable anomalous Hall effect: Berry curvature probe at oxides interfaces, *Phys. Rev. B* **106**, 075430 (2022).
 - [20] M. Trama, V. Cataudella, C. A. Perroni, F. Romeo, and R. Citro, Tunable Spin and Orbital Edelstein Effect at (111) $\text{LaAlO}_3/\text{SrTiO}_3$ Interface, *Nanomaterials* **12**, 10.3390/nano12142494 (2022).
 - [21] M. Trama, V. Cataudella, C. A. Perroni, F. Romeo, and R. Citro, Effect of Confinement and Coulomb Interactions on the Electronic Structure of the (111) $\text{LaAlO}_3/\text{SrTiO}_3$ Interface, *Nanomaterials* **13**, 10.3390/nano13050819 (2023).
 - [22] M. Trama, V. Cataudella, and C. A. Perroni, Strain-induced topological phase transition at (111) SrTiO_3 -based heterostructures, *Phys. Rev. Research* **3**, 043038 (2021).
 - [23] C. Liu, X. Zhou, D. Hong, B. Fisher, H. Zheng, J. Pearson, J. S. Jiang, D. Jin, M. R. Norman, and A. Bhattacharya, Tunable superconductivity and its origin at KTaO_3 interfaces, *Nature Communications* **14**, 951 (2023).
 - [24] X. Chen, T. Yu, Y. Liu, Y. Sun, M. Lei, N. Guo, Y. Fan, X. Sun, M. Zhang, F. Alarab, V. N. Strocov, Y. Wang, T. Zhou, X. Liu, F. Lu, W. Liu, Y. Xie, R. Peng, H. Xu, and D. Feng, Orientation-dependent electronic structure in interfacial superconductors $\text{LaAlO}_3/\text{KTaO}_3$, *Nature Communications* **15**, 7704 (2024).
 - [25] X. Cao, M. Zhang, Y. Wang, M. Qin, Y. Zhou, and Y. Xie, Geometric Control of Pairing: Universal Scaling of Superconductivity at KTaO_3 Interfaces, *arXiv preprint arXiv:2512.10301* (2025).
 - [26] D. Maryenko, I. Maznichenko, S. Ostanin, M. Kawamura, K. Takahashi, M. Nakamura, V. Dugaev, E. Y. Sherman, A. Ernst, and M. Kawasaki, Superconductivity at epitaxial LaTiO_3 - KTaO_3 interfaces, *APL Materials* **11** (2023).
 - [27] K. Ueno, S. Nakamura, H. Shimotani, H. T. Yuan, N. Kimura, T. Nojima, H. Aoki, Y. Iwasa, and M. Kawasaki, Discovery of superconductivity in KTaO_3 by electrostatic carrier doping, *Nature Nanotechnology* **6**, 408 (2011).
 - [28] L. Chen, S. Zhou, D. Tian, Y. Xiao, Q. Gao, Y. Wang, Y. Chen, F. Hu, B. Shen, J. Sun, *et al.*, Two-dimensional superconductivity at the $\text{CaZrO}_3/\text{KTaO}_3$ (001) heterointerfaces, *arXiv preprint arXiv:2507.01392* (2025).
 - [29] Z. Chen, Z. Liu, Y. Sun, X. Chen, Y. Liu, H. Zhang, H. Li, M. Zhang, S. Hong, T. Ren, C. Zhang, H. Tian, Y. Zhou, J. Sun, and Y. Xie, Two-Dimensional Superconductivity at the $\text{LaAlO}_3/\text{KTaO}_3$ (110) Heterointerface, *Phys. Rev. Lett.* **126**, 026802 (2021).
 - [30] Y. Gan, F. Yang, L. Kong, X. Chen, H. Xu, J. Zhao, G. Li, Y. Zhao, L. Yan, Z. Zhong, Y. Chen, and H. Ding, Light-Induced Giant Rashba Spin-Orbit Coupling at Superconducting KTaO_3 (110) Heterointerfaces, *Advanced Materials* **35**, 2300582 (2023).
 - [31] U. Filippozzi, G. Kimbell, D. Pizzirani, S. M. Walker, C. Cocchi, S. Gariglio, M. Gabay, S. Wiedmann,

- and A. D. Caviglia, High-field superconductivity from atomic-scale confinement and spin-orbit coupling at (111) $\text{LaAlO}_3/\text{KTaO}_3$ interfaces, [arXiv preprint arXiv:2411.05668](#) (2024).
- [32] L. Cheng, J. Liu, T. Liu, P. Chen, M. Zhang, J. Li, S. Zhang, F. Ye, Q. Wang, W. Liu, *et al.*, Interplay of spin-orbit coupling and trigonal crystal field enhances superconductivity in $\text{LaAlO}_3/\text{KTaO}_3$ (111), [arXiv preprint arXiv:2511.15526](#) (2025).
- [33] M. D. Dong, X. B. Cheng, M. Zhang, and J. Wu, Strongly coupled interface ferroelectricity and interface superconductivity in amorphous $\text{LaAlO}_3/\text{KTaO}_3$ (111), *Nature Communications* **10.1038/s41467-026-69641-4** (2026).
- [34] G. Kimbell, U. Filippozzi, S. Gariglio, M. Gabay, A. Glatz, A. Varlamov, and A. Caviglia, Electric field control of superconducting fluctuations and quasiparticle interference at oxide interfaces, [arXiv preprint arXiv:2601.02473](#) (2025), [arXiv:2506.17056 \[cond-mat.supr-con\]](#).
- [35] J. Kim, M. Yu, A. Omran, J. Yang, R. Ramachandran, W. O. Nachlas, P. Irvin, J. Levy, and C.-B. Eom, Enhanced Superconductivity at Quantum-Critical KTaO_3 Interfaces, [arXiv preprint arXiv:2601.02473](#) (2025), [arXiv:2511.12904 \[cond-mat.supr-con\]](#).
- [36] J. Zhai, T. Oh, H. Liu, C. Pan, N. Nagaosa, P. He, and J. Shen, Nonreciprocal Transport in KTaO_3 -Based Interface Superconductors with Parity Mixing, *Phys. Rev. Lett.* **134**, 236303 (2025).
- [37] X. B. Cheng, M. Zhang, Y. Q. Sun, G. F. Chen, M. Qin, T. S. Ren, X. S. Cao, Y. W. Xie, and J. Wu, Electronic nematicity in interface superconducting $\text{LAO}/\text{KTO}(111)$, *Phys. Rev. X* **15**, 021018 (2025).
- [38] H. Zhang, Y. Xiao, Q. Gao, N. Wu, S. Zhou, Y. Wang, M. Wang, D. Tian, L. Chen, W. Qi, D. Zheng, J. Zhang, F. Han, H. Yang, B. Liu, Y. Chen, F. Hu, B. Shen, J. Sun, W. Zhao, and J. Zhang, Magnetotransport evidence for the coexistence of two-dimensional superconductivity and ferromagnetism at (111)-oriented $\text{a-cazro}_3/\text{ktao}_3$ interfaces, *Nature Communications* **16**, 3035 (2025).
- [39] G. Zhang, L. Wang, J. Wang, G. Li, G. Huang, G. Yang, H. Xue, Z. Ning, Y. Wu, J.-P. Xu, Y. Song, Z. An, C. Zheng, J. Shen, J. Li, Y. Chen, and W. Li, Spontaneous rotational symmetry breaking in KTaO_3 heterointerface superconductors, *Nature Communications* **14**, 3046 (2023).
- [40] K. V. Shanavas, Z. S. Popović, and S. Satpathy, Theoretical model for Rashba spin-orbit interaction in d electrons, *Phys. Rev. B* **90**, 165108 (2014).
- [41] P. Bruneel, *Electronic and spintronic properties of the interfaces between transition metal oxides*, Ph.D. thesis, Université Paris-Saclay (2020).
- [42] M. R. Norman, Superconductivity from the Slater mode: Application to KTaO_3 heterostructures, [arXiv preprint arXiv:2601.02473](#) (2026), [arXiv:2601.10903 \[cond-mat.supr-con\]](#).
- [43] M. Trama, V. Könye, I. Cosma Fulga, and J. van den Brink, Self-consistent surface superconductivity in time-reversal symmetric Weyl semimetals, *Phys. Rev. B* **112**, 064514 (2025).
- [44] L. Lepori, D. Giuliano, A. Nava, and C. A. Perroni, Interplay between singlet and triplet pairings in multiband two-dimensional oxide superconductors, *Phys. Rev. B* **104**, 134509 (2021).
- [45] A. Nava, C. A. Perroni, R. Egger, L. Lepori, and D. Giuliano, Lindblad master equation approach to the dissipative quench dynamics of planar superconductors, *Phys. Rev. B* **108**, 245129 (2023).
- [46] A. Nava, C. A. Perroni, R. Egger, L. Lepori, and D. Giuliano, Dissipation-driven dynamical topological phase transitions in two-dimensional superconductors, *Phys. Rev. B* **109**, L041107 (2024).
- [47] J. C. Slater and G. F. Koster, Simplified LCAO Method for the Periodic Potential Problem, *Phys. Rev.* **94**, 1498 (1954).
- [48] E. A. Martínez, J. Dai, M. Tallarida, N. M. Nemes, and F. Y. Bruno, Anisotropic electronic structure of the 2d electron gas at the $\text{alox}/\text{ktao}_3(110)$ interface, *Advanced Electronic Materials* **9**, 2300267 (2023).
- [49] O. Copie, V. Garcia, C. Bödefeld, C. Carrétéro, M. Bibes, G. Herranz, E. Jacquet, J.-L. Maurice, B. Vinter, S. Fusil, K. Bouzehouane, H. Jaffrès, and A. Barthélémy, Towards Two-Dimensional Metallic Behavior at $\text{LaAlO}_3/\text{SrTiO}_3$ Interfaces, *Phys. Rev. Lett.* **102**, 216804 (2009).